

Questing for Minute Traces of Molecular Gas in
Circumstellar Debris Disks:
AU Microscopii and 49 Ceti Edition

Zachary S. Lambros

Faculty Advisor: A. Meredith Hughes

A Dissertation submitted to the
faculty of Wesleyan University
in partial fulfillment of the requirements for the
Degree of Master of Arts

Acknowledgments

First and foremost thank you, Meredith. This is as much your product as it is mine, and I could not be more thankful for everything you have given me...from teaching me how to science to the weekly pep-talks. Thank you for showing me the world beyond our own.

Thank you to the Wesleyan Astronomy Department who welcomed me in and gave me a home, and to all of my teachers who believed in me and gave all of themselves for the pursuit of education.

Special thanks to Luca Matrà for your help and for laying the foundation of my work.

Thank you Dad, Mom, and K for your love and support; 'At the end all that's left is family.'

Roy- I'm sorry for breaking everything, I didn't do it.

OG Basement Crew- Never forget to import pandas pandas pandas.

David and Robin - I would not be here without you. Thank you.

Contents

Contents	iii
List of Figures	v
List of Tables	xiii
1 Introduction	1
1.1 Circumstellar Disk Components	2
1.2 Debris Disks	5
1.3 AU Mic and 49 Ceti	10
2 Observations	13
2.1 AU Mic CO(2-1)	15
2.2 49 Ceti	17
3 Models	20
3.1 Keplerian Rotation Spectral Method	21
3.2 Spectral Spatial Shift	29
4 Results	41
4.1 Total Flux	41
4.2 Gas Mass	44
4.3 Exocometary Ice Mass Fraction and Line Ratio	48

5	Discussion	51
5.1	Comparison of Results	51
5.2	Primordial or Exocometary?	54
6	Conclusion	59
	Bibliography	63

List of Figures

1.1	(a) Protoplanetary disk Elias 2-27 imaged in the radio by ALMA. Notice the thickness and apparent density of the rings. (b) Two debris disks, AU Mic and HD107146, imaged in the visible band by HST. The thinner disk appearance compared to (a) is due to the lack of dense gas, while the color difference is due to the wavelength the disks were observed in. As smaller dust grains scatter better in the blue than in the red wavelength, the red color of the protoplanetary disk (a) is due to the observations being conducted in that wavelength. Both disk types contain similar grain sizes, but the number density of grains per volume varies.	2
1.2	Protoplanetary disk cross section showing density and temperature profiles around a $1 M_{\odot}$ star sampled at the millimeter and infrared wavelengths. Notice the change in temperature from the hot outer layer filled with gas to the cold inner midplane with a depletion of gas, which will transition into a debris disk (Dutrey et al., 2014; Reipurth et al., 2007).	4

1.3	Theoretical circumstellar disk models (Roberge and Kamp, 2010) using modeling methods from (Dullemond et al., 2001). The leftmost parabola shows the star’s blackbody flux, and the three rightmost peaks show different emission due to disks around the star. The largest peak (solid line) is from a protoplanetary disk, the middle peak (large dashed line) is from a transition disk, and the lowest peak (small dashed line) is from a debris disk. The local minimum of each line after it breaks away from the stellar blackbody shows the excess IR emission, which is at shorter wavelengths for protoplanetary disks than debris disks. Finally, note the overall fractional luminosity difference between protoplanetary disks ($L_{IR}/L_* = 0.2$) and debris disks ($L_{IR}/L_* = 0.0015$).	6
1.4	Radio telescope dishes in the Atacama Large Millimeter/submillimeter Array (ALMA), one of the most sensitive radio interferometers on Earth in its wavelength. SOURCE: ALMA Observatory	7
2.1	Velocity channel maps for AU Mic, showing flux density (Jy) per beam values per velocity space for CO(2-1). The lower left image shows the beam size (lower right hand corner), scale bar (upper right hand corner), and velocity channel (upper left hand corner). The scale bar represents 10 au. The beam size from the naturally weighted combined image is $1.22'' \times 0.71''$. The seemingly random scattering of noise shows no clear presence of gas, which one would be able to observe in the form of a ‘butterfly’ pattern (see 49 Ceti observations). The zero-point axes labels for RA and Dec refer to the pointing center of the observation, centered around the location of the star (shown as a small black star in the center of each channel).	16

2.2	The Moment 0 and Moment 1 maps for AU Mic. The naturally weighted beam size is located in the bottom right, and a scale bar representing 10 au is in the upper right. The center of the images (RA = 0, Dec = 0) are the pointing centers of the observations located at the star. (a) The lack of any apparent disk structure indicates little-to-no gas presence. (b) As there is seemingly no disk structure in the Moment 0 map (a), there is likely no clear velocity field structure. Notice the large unit size on the colorbar, an artifact of a lack of signal and attributed to a few random pixels. The majority of pixels contain velocities within $\pm 20 \text{ km s}^{-1}$ of the star's systemic velocity. .	17
2.3	Velocity channel maps for 49 Ceti CO(3-2) (a) and HCN(4-3) (b), showing flux density (Jy) per beam values per velocity space. The lower left image shows the beam size (lower right hand corner) and scale bar (upper right hand corner). The scale bar represents 100 au. The black marker in the center of each channel represents the location of the star. The random scattering of noise and lack of a distinct butterfly pattern in the HCN maps (b), as compared to channel maps for CO (a), indicates that scarce amounts (if any) of HCN is present in the disk.	18

- 2.4 The Moment 0 maps for 49 Ceti (a) CO(3-2), (b) HCN(4-3), and (c) Moment 1 map of CO(3-2) for 49 Ceti. The naturally weighted beam size is located in the bottom right, and a scale bar representing 100 au is in the upper right. The center of the images (RA = 0, Dec = 0) are the pointing centers of the observations located at the star. (a) The beautiful disk structure shows a nice presence of gas equally distributed along both sides of the disk along the major axis (b) The lack of gas signal is quite evident here, similar to the Moment 0 map seen for AU Mic (Figure 2.2.a) (c) As there was clear disk structure for the Moment 0 map for CO(3-2), we are able to see the velocity field of the gas. Pay close attention to the units - as the star has a systemic velocity of 2.78 km s^{-1} all of the velocity values are shifted accordingly, explaining why the center of the disk does not have $V = 0 \text{ km s}^{-1}$. 19
- 3.1 Keplerian velocity fields calculated for geometrically thin disks viewed at different inclination angles. (a) shows an example of a nearly face-on disk ($i = 30^\circ$), while the (b) shows an example of a disk viewed close to edge-on ($i = 80^\circ$). 23
- 3.2 Keplerian velocity fields from for a single channel, with LOS velocities between $1 - 1.5 \text{ km s}^{-1}$. The disk parameters are the same as those of Figure 3.1.a, with an inclination of $i = 30^\circ$. Notice that this model is the same butterfly pattern seen in channel maps with large amounts of signal. . . . 24
- 3.3 (a) The log flux density power-law brightness profile for a debris disk with the same parameters as Figure 3.1.a and 3.2, with $i = 30^\circ$. A power-law of $x_{pwr} = 1.5$ was used for this specific model. We restrict our model to a radius of $< 200 \text{ au}$ from the star, or central pixel. (b) The log flux density power-law brightness profile for a single velocity channel of $1 - 1.5 \text{ km s}^{-1}$ for a debris disk with the same parameters as (a). 25

3.4	Flux density vs velocities for a most basic stellar debris disk model using the Keplerian velocity fields from Figure 3.1(left panel) and the power-law flux brightness profile from Figure 3.3.a. Integrating flux per velocity channels, as seen in Figure 3.3.b, provides integrated flux density values for each 0.5 km s^{-1} channel of velocities. The ‘double peak’ structure with a local minimum at 0 km s^{-1} signifies the blue and redshift portions of the disk. . .	26
3.5	χ^2 value as a function of integrated flux for the AU Mic observations of CO(2-1). The χ^2 values increase from the minimum value at a flux of 0.0 Jy km s^{-1} (blue line), and the $\Delta\chi^2$ difference at $\sim 0.07 \text{ Jy km s}^{-1}$ corresponds to a 3-sigma upper limit on the flux (red dashed line).	28
3.6	Spectrum of CO(3-2) emission from the disk around 49 Ceti for a single pixel at a position offset of (0.32,1.68) arcsec relative to the disk center.	30
3.7	Spectrum of CO(3-2) emission from the disk around 49 Ceti for a single pixel at a position offset of (0.32,1.68) arcsec relative to the disk center. This spectrum illustrates the predictable velocity offset of the emission from the systemic velocity of the source, due to the Keplerian rotation of the disk around the star. The spectral shift method applies an offset along the velocity axis to shift the emission in every pixel into the zero-velocity channel, in order to concentrate the signal and thereby maximize the SNR of the data. The spectrum after the shift (orange line) is not quite located at the desired velocity of $V = 0 \text{ km s}^{-1}$ due to the lack of precision between the Keplerian model velocity field and the velocity field of the data.	31

- 3.8 Spectrum of CO(3-2) emission from the disk around 49 Ceti, both before (a) and after (b) a spectral-spatial shift is applied. The spectrum showcase the ability of the model to shift multiple pixels by corresponding velocity field values in the same method as Figure 3.8. The shift is applied to spectrum for 40 random pixels at position offsets of $0 - 0.4$ and $1.6 - 2.0$ arcsec relative to the disk center using known velocities from CO(3-2) detections. Pixels are shifted to a single channel with a velocity of 0 km s^{-1} 32
- 3.9 Velocity channel maps for 49 Ceti CO(3-2) both before (a) and after (b) a spectral shift method was applied to the data, shown as flux density (Jy) per beam values per velocity space. The lower left image shows the beam size (lower right hand corner) and scale bar (upper right hand corner). The scale bar represents 100 au. The bright ‘butterfly’ pattern in (a) is integrated together into only a few channels in (b) located around $V = 0 \text{ km s}^{-1}$. The effectiveness of the method is seen both in these two panels as well as in the fringe panels, which showcase large amounts of random scattered noise. The star’s location is shown by the green marker, perfectly at the center of emission. 34
- 3.10 Varying velocity fields for 49 Ceti with a single contour line at the systemic velocity of $V_{sys} = 2.78 \text{ km s}^{-1}$ (Hughes et al., 2017). The left panel shows a velocity field created using simple Keplerian rotation with a disk inclination and position angle; the central panel’s velocity field is obtained using the velocity locations of the max flux signal peak in each pixel spectrum; the right panel’s velocity field is from a standard Moment 1 map (intensity-weighted coordinate velocity fields). The scale bar in the top right hand corner of the right panel represents 100 au. Notice that the single contour lines of the systemic velocity lie almost directly along the semi-minor axis of the disk, as expected. 36

3.11	Molecular line spectral flux shifting for 49 Ceti CO(3-2) by velocity source: Moment 1 map (green dashed), Peak known CO(3-2) (blue dashed), Keplerian model (red dashed), plus the un-altered spectrum from the original data (solid blue). Notice the varying widths and peaks of the different velocity methods, with a higher peak and minimal line spreading corresponding to a larger SNR.	37
3.12	(a) Standard Keplerian velocity field of a close-to edge-on ($i = 89^\circ$) debris disk. We see that the disk is flattened dramatically at higher inclinations, which would be unable to accurately describe the velocity vectors of any gas in a puffy edge-on disk. (b) Keplerian velocity field of a close-to edge-on ($i = 89^\circ$) debris disk using linear velocities away from a single semi-major axis and ignoring the minor axis. In an edge-on disk it is hoped that a linear velocity field would be better suited to detail gas velocities above and below the midplane of the disk, thus accounting for the ‘puffiness.’ Unfortunately, as AU Mic shows no detectable signal we are only currently able to show that the linear velocity field produces the same upper limit as a standard Keplerian rotation field.	40
4.1	Spectrum of AU Mic CO(2-1) from an 8×8 arcsecond box centered at the pointing center of our observations: un-altered (green), using the spatial-spectral shifting method assuming the NW corner is blueshifted towards us (blue), and using the spatial-shifted method assuming the NW corner is redshifted away from us (red). Signs of a detection would show up as a peak in the shifted spectrum (blue or red line) located at $V_{LSRK} = 0$, similar to the central peaks in Figure 3.11. The lack of this central peak, in addition to random peaks and valleys indicates no detectable signal.	42

4.2	Spectrum of HCN(4-3) from an 8×8 arcsecond box centered at the pointing center of our observations: un-altered (green), altered with a spectral flux shifting method (blue). We only apply a single shift as we have velocity fields from previous detections of CO indicating that the NE side of the disk is redshifted away from us. Signs of a detection would appear as a peak in the shifted spectrum (blue or red line) located at $V_{LSRK} = 0$, similar to the central peaks in Figure 3.11.	43
4.3	(a) Calculated LTE gas mass upper limits for a range of excitation temperatures based on possible theoretical temperatures found in debris disk systems and previous constraints on temperatures from gas detections in other systems. T_{ex} rises with CO mass due to Boltzmann statistics that define the number of molecules occupying higher energy states and higher temperatures (b) Calculated NLTE gas mass upper limits for a range of T_k and electron (e^-) densities. As NLTE is not described by the same collisional transitions as LTE it is necessary to use T_k values instead, as $T_{ex} \neq T_k$ in NLTE. The right side of the plot shows where the electron density is high enough to produce collisional transitions and describe the system in LTE, matching with our calculations from (a). Calculations for NLTE mass limits were performed by Luca Matr�.	47
5.1	A compilation of debris disks with line flux detections or upper limits of CO(3-2 or 2-1) normalized to a distance of 100 pc as a function of spectral type and stellar age. The majority of detections occur at young stellar ages and more massive (AB) spectral types. FGK detections are also connected to younger stars, but appear to have much lower line fluxes. The upper limits seem to have no consistent grouping and are widespread across the plot. Our scaled upper limit on CO(2-1) in AU Mic is circled in red in the lower left hand corner. One can see just how low it really is compared to other upper limits and detections. The figure is taken from Hughes et al. (2018).	53

List of Tables

2.1	AU Mic Observational Parameters	14
2.2	49 Ceti Observational Parameters	15
3.1	Free parameters for our two sources, AU Mic and 49 Ceti. The line break in the middle separates the stellar parameters (above) and the disk parameters (below). Superscripts indicate the source, which is listed at the bottom. . .	22
3.2	The SNR statistics for the central channels (peaks) in Figure 3.11 based on the different velocity fields used. As expected from Figure 3.11, a larger certainty and precision in velocity field values directly relates to a higher SNR. Moreover, we effectively show that the inclusion of spatial/velocity distributions directly affects the SNR and sensitivity of total integrated flux measurements.	37
4.1	Input parameters and constants used to calculate an upper limit on total gas mass assuming LTE. Note that we use a range of excitation temperatures (T_{ex}) as the exact temperature is unknown. Superscript letters to the left of the value indicate the source of the value, listed at the bottom of the table.	45

4.2	Input parameters and constants used to calculate an upper limit on total gas mass for 49 Ceti HCN(4-3) assuming LTE. Note that, unlike for AU Mic, we are able to use a single excitation temperature (T_{ex}) as constrained in previous observations. Superscript letters to the left of the value indicate the source of the value, listed at the bottom of the table.	48
4.3	Input parameters used to calculate an exocometary ice mass fraction for CO+CO ₂ in AU Mic. We assume that the nature of the gas is secondary and expelled in the form of exocometary outgassing. Superscript letters to the left of the value indicate the source of the value, listed at the bottom of the table.	49

CHAPTER 1

INTRODUCTION

*They called not my name or shape but only to tell of an
untold world hidden in the carry of a dark current. 'Be
bold,' they said, but I had already forgotten my misfortunes
sunk once before and stepped blindly into the water...*

The study of circumstellar disks presents an opportunity to study stellar and planetary evolution. Their existence around young stars and their physical parameters create a petri dish in astronomy in which it is possible to understand the development of a system and in doing so, develop an understanding of necessary processes to form larger planetary bodies in orbit around a central star. By basic definition, a circumstellar disk is material of dust and/or gas, rotating around a central stellar source in Keplerian rotation. Imagine the asteroid or Kuiper belts, our solar system's very own version of a disk. The broad category of circumstellar disks can then further be broken down into two main types: protoplanetary and debris. Sample images of debris disks and protoplanetary disks observed at both infrared and radio wavelengths are shown in Figure 1.1. Even though their shapes and geometry are comparable, notice the major difference in thickness and structure. Protoplanetary disks are 'puffier' due to the gas component comprising 99% of the disk's mass. In order to keep hydrostatic equilibrium the gas is supported against gravity by pressure, which puffs out the disk. Debris disks,

which are mostly dust by mass, do not have the same pressure support, resulting in a vertically flatter disk. In each we see that the dynamics of the disk are dominated by the material composition of the disk, be it majority gas or dust. The differing types of disks also have specific connections to planets; protoplanetary disks host the formation of planets while debris disks are signposts of mature planetary systems where planet formation has proceeded to at least the stage of Pluto-like planetesimals. While we only directly deal with circumstellar debris disks in the body of this paper, we shall explore the basic characteristics of both types and their respective roles in the study of disks.

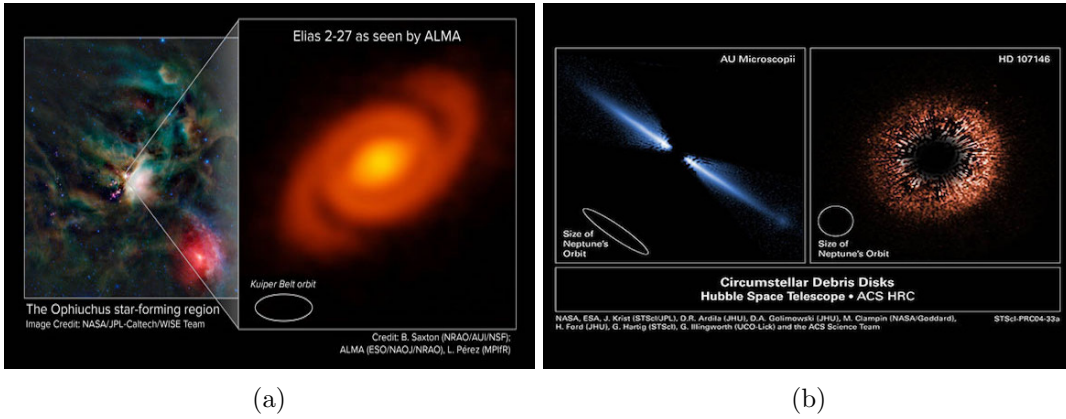


Figure 1.1: (a) Protoplanetary disk Elias 2-27 imaged in the radio by ALMA. Notice the thickness and apparent density of the rings. (b) Two debris disks, AU Mic and HD107146, imaged in the visible band by HST. The thinner disk appearance compared to (a) is due to the lack of dense gas, while the color difference is due to the wavelength the disks were observed in. As smaller dust grains scatter better in the blue than in the red wavelength, the red color of the protoplanetary disk (a) is due to the observations being conducted in that wavelength. Both disk types contain similar grain sizes, but the number density of grains per volume varies.

1.1 Circumstellar Disk Components

In the basic stellar evolution model, stars form a protoplanetary disk first during stellar formation, before later transforming into a debris disk. A protoplanetary disk is formed first while the star is still engaged in active formation, at which time a mass of material

with a ratio of 100:1 part gas to dust (Knapp and Kerr, 1974) accretes around the star. While the accreted material remains in orbit about the star due to conservation of angular momentum, the weight of the material induces gravity and causes the material to collapse down under its own weight to form a flattened disk. If larger bodies of dust are able to achieve critical mass, $\sim 10 M_{\oplus}$ (Inaba et al., 2003; Perri and Cameron, 1974), they can attract gas during the protoplanetary stage to form gas giant planets. The gas-heavy disk (99% of the total mass) is made up of mostly H_2 (Bergin and Williams, 2017), is puffy in thickness and appearance, and varies in temperature throughout the disk, with direct heating of the disk occurring on the edges of the disk. As you move towards the midplane the material cools off to only a few Kelvin, as it is shielded from stellar radiation by the dense material around it (D'Alessio et al., 2005). Figure 1.2 (Dutrey et al., 2014; Reipurth et al., 2007) shows the temperature and density structure in relation to physical location in the disk around a $1 M_{\odot}$ star as sampled radially by both ALMA (millimeter) and Herschel (infrared). Notice the three important distinct gas layers in the disk as pointed out by roman numerals. As a protoplanetary disk is heavily dominated by gas, its many properties are determined by a combination of thermal pressure, turbulence, gas viscosity, and magnetic fields, as well as the usual stellar radiation, gravity, and rotation inherent in a disk (Dullemond et al., 2007; Dutrey et al., 2014).

It was typically believed that the transition from protoplanetary to debris depends solely on the age of the star, taking place around the 10 million year (Myr) mark (Isella et al., 2012). However, recent surveys note that the transition and distinction between the two disk types depends more on the excess infrared emission present in the disk. As protoplanetary disk mass and surface density decrease over time in general (Wyatt et al., 2015), the specific timescale for the demise of a protoplanetary disk can be estimated using the disk fraction, the percentage of stars with disks in a young cluster (Ohsawa et al., 2015). It is observed that the disk fraction drops off exponentially with time at a constant time of 2.5 Myr (Mamajek, 2009). Recent models indicate

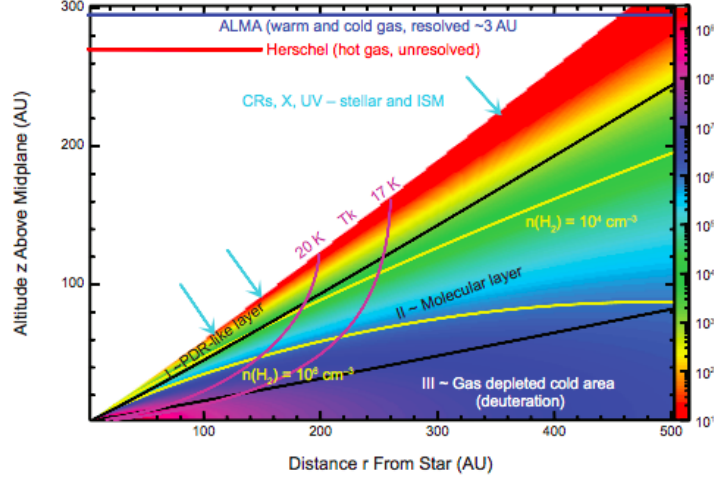


Figure 1.2: Protoplanetary disk cross section showing density and temperature profiles around a $1 M_{\odot}$ star sampled at the millimeter and infrared wavelengths. Notice the change in temperature from the hot outer layer filled with gas to the cold inner midplane with a depletion of gas, which will transition into a debris disk (Dutrey et al., 2014; Reipurth et al., 2007).

that the disk fraction drop off is determined by the initial disk mass function (Ohsawa et al., 2015). As the dispersal of a protoplanetary disk is not completely consistent with time it is therefore important to instead note that protoplanetary disks are dominated by accretion and have a higher optical depth exceeding $\tau = 1$ at optical wavelengths ($\tau < 1$ at mm wavelengths), while debris disks are dominated by the expulsion and destruction of material and have an optical depth of $\tau < 8 \times 10^{-3}$ (chosen specifically from HD 141569 to serve as the exact transition between a protoplanetary and debris disk (Hughes et al., 2018; Wyatt et al., 2015). As disks come in a variety of radial sizes and masses this accounts for the observation and discovery of debris disks in systems younger than 10 Myr (Carpenter et al., 2009; Espaillat et al., 2017). When the transition from the protoplanetary to debris stage does occur, the general process involves most, if not all, of the gas either being accumulated onto the star or expelled out of the system through the processes of accretion, photoevaporation, or stellar winds (Hollenbach et al.,

1994; Williams and Cieza, 2011). The remaining dust, which is consistently hotter than dust in a protoplanetary disks due to the lack of dust shielding (Matthews et al., 2014), collides together to create more dust of smaller grain sizes. This destructive process, known as the collisional cascade (Dohnanyi, 1969; Pan and Schlichting, 2012), stirs up planetesimals and debris causing them to collide and even break apart some of the larger planetesimals that form and agglomerate during the protoplanetary stage. We also see that debris disks are far fainter than protoplanetary (primordial) disks, due to the agglomeration of material in the system into larger planetesimals, which overall encompass a smaller surface area than widespread dust. Looking internally, we see two debris disks within our own solar system, in the Kuiper Belt and Zodiacal Light (Nesvorný et al., 2010, 2011)!

1.2 Debris Disks

1.2.1 Observing Debris Disks

Regarded as a completely different object, debris disks seem to be an inverse of protoplanetary disks, dominated by dust rather than gas and low fractional luminosity ($\sim 100\times$ fainter) compared to protoplanetary disks (Matthews et al., 2014). Fractional luminosity of the dust, $f_d = L_{IR}/L_*$, is usually found on the order of $10^{-3} - 10^{-6}$ (Hillenbrand et al., 2008; Moór et al., 2011; Siegler et al., 2007). Detection of debris disks in particular are the result of large surveys aimed at measuring excess infrared emission where debris disks peak in stellar SEDs. Figure 1.3 depicts different circumstellar disk models, similar to SEDs, for three different types of disks: protoplanetary, transitional, and debris. We see that debris disks are most readily detected at mid-IR wavelengths, whereas protoplanetary disks are also typically bright at near-IR wavelengths as shown by the local minimum branching off of the stellar blackbody curve. Early detection rates indicated that 15% of main sequence stars contained debris disks (Aumann, 1985). More recent surveys with higher sensitivity have been able to expand

this value out by spectral type, noting detection rates by spectral class to be 20 – 30% for A stars (Rhee et al., 2007; Thureau et al., 2014) and 17 – 20% for solar-type stars (Montesinos et al., 2016; Sibthorpe et al., 2018) with a higher rate around F stars than G,K stars. M stars show very low detection rates, with the highest rates valued at < 13% (Lestrade et al., 2006) and references within (Wyatt, 2008). This low M star rate is believed to be due to multiple effects, such as dust grain removal from stellar winds (Plavchan et al., 2005), low sensitivity of M star fractional luminosities (Morey and Lestrade, 2014), and differing minimum mass solar nebula (Gaidos, 2017). Trilling et al. (2008) and Montesinos et al. (2016) also note that the declining detection rate from A to M spectral types could be linked to age of the system.

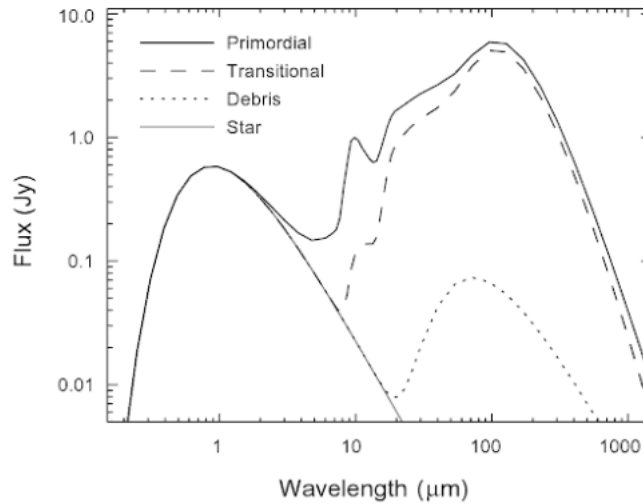


Figure 1.3: Theoretical circumstellar disk models (Roberge and Kamp, 2010) using modeling methods from (Dullemond et al., 2001). The leftmost parabola shows the star’s blackbody flux, and the three rightmost peaks show different emission due to disks around the star. The largest peak (solid line) is from a protoplanetary disk, the middle peak (large dashed line) is from a transition disk, and the lowest peak (small dashed line) is from a debris disk. The local minimum of each line after it breaks away from the stellar blackbody shows the excess IR emission, which is at shorter wavelengths for protoplanetary disks than debris disks. Finally, note the overall fractional luminosity difference between protoplanetary disks ($L_{IR}/L_* = 0.2$) and debris disks ($L_{IR}/L_* = 0.0015$).

Although these wide infrared surveys have the ability to detect the presence of a debris disk, due to the low excitation temperature of the gas (< 100 K) it is beneficial to observe the disk at the millimeter wavelength to detect low energy gas rotational transitions. At the millimeter wavelength, the use of radio interferometry increases the spatial resolution by linking up a number of radio dishes spaced out at varying baselines, or distances between any two antennas in the array (K. Rohlfs, 2000). Interferometry essentially creates a giant telescope out of a number of smaller telescopes by interfering incoming signals from different dishes to synthesize it as a large single telescope. One of the best radio interferometers currently on Earth is the Atacama Large Millimeter/submillimeter Array (ALMA) (Figure 1.4) located in the most arid non-polar desert on the planet at an altitude of around 16,500 ft above sea level. The need for a sensitive radio interferometer is due to the benefit of observing debris disks at the millimeter wavelength, which probes both of the main components of the disk: thermal emission from dust and rotational transitions of small gas molecules. Additionally, the sensitivity of ALMA specifically has created new possibilities for the detection of gas in debris disks which was often too faint to be detected with less-sensitive telescopes.



Figure 1.4: Radio telescope dishes in the Atacama Large Millimeter/submillimeter Array (ALMA), one of the most sensitive radio interferometers on Earth in its wavelength. SOURCE: ALMA Observatory

1.2.2 Gas in Debris Disks

While the presence of debris disks is relatively well known and constrained due to dust, searches for gas in these disks has yielded only a handful of detections. The resulting gas constituent was often unknown due to sensitivity limitations of instruments. As gas in debris disks is quite clearly much fainter than in protoplanetary disks, long integration times were necessary to pick up any traces of gas. But thanks to improved sensitivity in millimeter and infrared instrumentation, that integration time has gone down drastically; and yet, debris disks in general are still observed to be gas-poor (Hughes et al., 2018). As of this year there are currently only 12 debris disks that contain detected (as opposed to an upper limit) CO rotational transition gas (Hughes et al., 2018). Additionally, only molecular CO emission lines have been observed in debris disks, which correlate to higher mass areas at a further radius from the star. Several individual atomic lines have been detected, but CO remains to date the only unambiguous *molecule* detected. It is important to note that there are limited detections of H₂ gas in debris disks (France et al., 2007) due to the relatively cold temperatures involved. Several claimed detections of H₂ (Carmona et al., 2008) have since been refuted. From surveys of specific bright debris disks it is estimated by (Moór et al., 2017) that 62 – 75% of dust-rich ($5 \times 10^{-4} < L_{\text{disk}}/L_{\text{bol}} < 10^{-2}$) A stars contain detections of CO. This compares quite drastically to the detection rates of intermediate FG stars, which is placed at $\sim 7\%$ from sources detected by Lieman-Sifry et al. (2016); Marino et al. (2016); Olofsson et al. (2016). It is still debated as to whether this lower detection rate around FGK stars is due to the reality of a lower incidence rate or if it is in fact a byproduct of lower CO line luminosities that are more difficult to detect with short integration times, in that current FGK gas detections are roughly two orders of magnitude fainter than detections around AB stars (Hughes et al., 2018). As our work presents the first search for molecular gas in an M star (previous studies have only prospected for atomic gas), it is too early to comment on the prevalence of gas in debris disks around low-mass stars.

Along with any detections of gas comes the need to determine its origin, be it primordial or secondary. Initial theories were keen to conclude that detections must point to either a primordial or secondary process for all debris disks. However, as more disks are sampled it seems increasingly probable that the presence of gas can be of either nature. A larger number of disks seem to exhibit definitive traces of secondary origin, such as β Pic (Matrà et al., 2017a), HD 181327 (Marino et al., 2016), η Corvi (Marino et al., 2017), and Fomalhaut (Matrà et al., 2017b). Of course, not all of these disks share the same exact gas-production method. Hughes et al. (2018) points out the varying possibilities for secondary gas creation in a debris disk, such as photodesorption (Grigorieva et al., 2007), collisions between icy dust grains (Czechowski and Mann, 2007), collisions between planetary embryos (Jackson et al., 2014), and/or desorption and sublimation from comets (Beust et al., 1990; Zuckerman and Song, 2012). Recent models provide a more complex look at a combination of these processes, such as in Kral et al. (2017), which models secondary gas production from both planetesimal collisions and photodissociation of CO into C and O. Processes for primordial gas production, on the other hand, are often described by large quantities of gas present and by the ‘not’ logic gate when attempting to prove secondary origin (ie, *not* secondary == primordial). Two disks in particular show signs of primordial gas: HD 21997 (Kóspál et al., 2013) and HD 131835 (Moór et al., 2015). The large amounts of CO found in the two disks is in the order of $10^{-2} - 10^{-3} M_{\oplus}$, about 4 – 5 orders of magnitude larger than other debris disks with secondary origins. The model used by Kral et al. (2017) is also keen on the primordial nature of gas in these two disks, showing the inability of secondary processes to produce the large quantities of gas observed in HD 21997 and HD 131835. These observations have also raised the scenario of a hybrid disk, in which primordial gas and secondary dust may coexist (Kóspál et al., 2013). As one can tell, there are an immense number of slushie flavor combinations for gas and dust in debris disks!

1.3 AU Mic and 49 Ceti

1.3.1 49 Ceti

The A1V star 49 Ceti (HD 9672) is located approximately 60 pc (van Leeuwen, 2007) away from us and contains a debris disk that has generated a plethora of interest over recent years. Sadakane and Nishida (1986) and Zuckerman et al. (1995) were the first to report infrared excess around the star from surveys of ‘Vega-like’ stars. 49 Ceti’s dust disk has been observed to be on the scale of 30 – 60 au for small grains and 60 – 200 au for larger grains and gas (Hughes et al., 2008; Wahhaj et al., 2007). It was also one of the earliest debris disks observed to contain molecular gas, in CO (Dent et al., 2005; Zuckerman et al., 1995). At the time of its discovery of gas 49 Ceti was just one of three debris disks with a clear CO double peak structure and strong line flux levels ($f > 10^{-3}$ Dent et al. (2005)). Early SMA observations indicate a CO gas mass in the order of $10^{-4} M_{\oplus}$ (Hughes et al., 2008). By resolving emission for the first time, these observations proved that gas is indeed in a Keplerian disk rotating around the star. Follow-up ALMA observations show similar integrated flux levels ($\sim 6 \text{ Jy km s}^{-1}$), implying a similar gas mass (Hughes et al., 2017). The high presence of gas in the disk compared to similar A star debris disks makes it a unique target for study, as it has the ability to give insights into the origin of gas in debris disks. Multiple attempts to categorize the origin have already been conducted in a number of different wavelengths, with a high emphasis on the exocometary presence within the disk (Higuchi et al., 2017; Miles et al., 2016; Roberge et al., 2014; Zuckerman and Song, 2012). Other studies aim to characterize the dust and gas structure within the disk in efforts to determine how the two interact in older disk systems¹ (Choquet et al., 2017; Hughes et al., 2017; Roberge et al., 2013). Measurements of H₂ in the system have proven minimal (Carmona et al., 2007) and thus instigates the need for investigation of other atomic/molecular species (Higuchi et al., 2017). Our goal expands on these studies, in which we aim to understand the true

¹The estimated age for 49 Ceti is ~ 40 Myr, placing it in the canonical ‘gas-poor’ debris disk category (Zuckerman and Song, 2012)

origin of the gas through observations of an additional molecule, HCN. Measurement of an HCN/CO molecular ratio allows for constraints on the chemical composition of the gas, which in turn may be compared to possible originators of the gas, be it secondary in nature such as from exocomets (Biver et al., 2002; Matr   et al., 2018) or primordial from protoplanetary disks (  berg et al., 2010). Of all disks to probe for HCN, 49 Ceti is an ideal candidate due to its high levels of CO gas. After all, if you want to find gas, is it not best to look for where there already is gas?

1.3.2 AU Mic

The popular M1Ve star AU Microscopii (AU Mic) has long been a source of study by astronomers due to its high solar activity and flaring, detailed by (Rodono et al., 1986) or any number of sources, in addition to its close proximity to Earth at only 9.9 pc (van Leeuwen, 2007). However, AU Mic has augmented its popularity in the astronomical community when an edge on debris disk was discovered (Kalas et al., 2004) in scattered light following excess submillimeter emission detections (Liu, 2004). The rare fact that the disk was seen in visible light inspired many initial studies in the visible and UV bands (Graham et al., 2007; Krist et al., 2005; Roberge et al., 2005), in addition to the traditional infrared and radio observational approach to disks (Metchev et al., 2005). Several factors inspired the next generation of studies, such as the disk’s similarity to the β Pic disk (Fitzgerald et al., 2007; Wilner et al., 2012), the edge-on orientation of the disk, as well as the fact that the disk is around an M star, which have not been well surveyed (Wyatt, 2008). The disk, as fitting with the stellar type, is smaller than its neighbors in the β Pictoris moving group, at a relatively well constrained radius of $8.8 - 40$ au (MacGregor et al., 2013; Matthews et al., 2015; Wilner et al., 2012). AU Mic is also a major candidate for hosting exoplanets, as there are several fast-moving structures seen throughout the disk (Boccaletti et al., 2018; Wang et al., 2015). Please note that the certainty on whether these features are exoplanets or other disturbances in the disk is still to be determined, as alternative theories suggest the root cause may be

stellar winds, magnetic fields, or dust grain expulsion (Chiang and Fung, 2017; Sezestre et al., 2017). The prevalence of these high stellar winds and X-ray activity (Schneider and Schmitt, 2010) naturally interact with the disk, which may be seriously affecting the structure and composition of the dust in the disk. Of course, the gas composition of the disk is quite unknown. Searches for H_2 have shown extremely low levels (Roberge et al., 2005), similar to what is observed in β Pic. Thus it is necessary to probe into the molecular gas nature of the debris disk around AU Mic. Current sensitivity allows us to conduct a deep search for CO in the disk, which, combined with the star's close proximity, will account for one of the most sensitive searches for gas in any debris disk system. As there is also a void in the sample of gas in M star debris disks our search for gas also provides some much needed depth into the presence of gas in M star debris disks. We are certain that gas is common in young A star debris disks, but without any information on M star debris disks we are completely in the dark! And as my father always says...‘it is better to light a candle than to curse the darkness.’

CHAPTER 2

OBSERVATIONS

*...laid bare on the Captain's table I see maps filled with
only blankness. It seeps into my eyes, breeding tears at the
beggar's chant, 'they say an empty chart leads but to the
Boatman, for he is the only true interpreter'...*

We observe both sources, AU Mic and 49 Ceti, using the Atacama Large Millimeter/submillimeter Array (ALMA) located on the Chajnantor plateau an altitude of ~ 16500 ft above sea level in Chile's Atacama Desert. There are 66 antennas in the array, with 54 of 12 meter diameter and the remaining 12 of 7 meter diameter. The antennas, which can each achieve a resolution of 20 arcseconds at the millimeter wavelength, can be placed anywhere up to 16 kilometers apart. It is important to note that the general procedure for reducing the observational data follows the same path. Raw data was calibrated for us in the standard ALMA pipeline to produce calibrated visibilities from each observational date. We then concatenated the different observational dates into a single file, one for each source. In CASA we use tasks `CVEL` and `UVCONTSUB` before `CLEAN` to produce image visibilities. `CVEL` converts the velocity axis from topocentric to a LSRK rest frame, while `UVCONTSUB` carries out a polynomial fit to specified line-free channels and subtracts the continuum emission to isolate the specific lines observed. Position-position-velocity channel maps are created with image sizes of

240×240 pixels and pixel sizes corresponding to $0.08''$ per pixel for AU Mic and $0.1''$ per pixel for 49 Ceti. The same scales are used to create Moment 0 and Moment 1 maps. Moment 0 maps are position-position representations of the integrated value of the spectrum, while Moment 1 maps are intensity weighted velocity fields. Channel maps were restricted to $\pm 20 \text{ km s}^{-1}$ of the source's systemic velocity. We use a systemic velocity of 2.78 km s^{-1} for 49 Ceti (Hughes et al., 2017) and 1.2 km s^{-1} for AU Mic (Dufloc et al., 1995). Tables 2.1 and 2.2 show the basic observational parameters for each of our two sources. We report the number of antennas used for the interferometer, observation time on the source, the pointing center of the observations, and the naturally weighted interferometer beam size. Additionally, the different calibrators are mentioned. Bandpass calibrators (bright quasars) are used to determine the baseline instrumental levels and sensitivity of channels; absolute flux calibrators (generally solar system objects or frequently monitored bright quasars) are observed to scale for the correct amplitudes; and gain calibrators (radio sources near the target) are observed on a rotating cycle with the target to account for atmospheric and instrumentation changes during the course of the observations. The pointing center RA and Dec refer to the right ascension and declination of the central pixel in the calibrated visibility observations, which varies slightly ($0.2 - 5$ arcseconds) from the known J2000 coordinates.

Parameter	26-March-2014	18-August-2014	24-June-2015
# Antennas	32	35	34
Bandpass Calibrator	J1924-2914	J2056-4714	J1924-2914
Absolute Flux Calibrator	Titan	J2056-472	Titan
Gain Calibrator	J2101-2933	J2101-2933, J2057-3734	J2056-3208, J2101-2933
Time on Source	27:26.4s	32:42.6s	32:42.6s
Naturally Weighted Beam Size ($''$)	0.44×0.31	0.32×0.29	1.22×0.71
Pointing RA	20:45:09.84	20:45:09.85	20:45:09.87
Pointing Dec	-31.20.32.37	-31.20.32.51	-31.20.32.82

Table 2.1: AU Mic Observational Parameters

Parameter	04-November-2013
# Antennas	28
Bandpass Calibrator	J0006-0623
Absolute Flux Calibrator	J0334-401
Gain Calibrator	J0132-1654
Time on Source	41:09s
Central Frequency of Spectral Windows (GHz)	CO(3-2): 345.7959899; HCN(4-3): 354.5054759; Continuum: 344; 357
Naturally Weighted Beam Size (")	0.59 x 0.44
Pointing RA	01:34:37.87
Pointing Dec	-15.40.34.94

Table 2.2: 49 Ceti Observational Parameters

2.1 AU Mic CO(2-1)

AU Mic was observed on three dates: 26-March-2014, 18-August-2014, and 24-June-2015, each with a total on-target time of approximately 30 minutes. Cycles between these on-source observations varied in length, ranging from 8-11 minutes. The observations were conducted using 12-meter diameters with baselines from 3 m to 1.5 km. Weather conditions show a stable PWV (Precipitable Water Vapor) at 0.63, 1.62, and 0.7 mm for the three dates, listed chronologically. We assume that our source is at the center of pointing, as proper motion offsets were applied to the J2000 coordinates. AU Mic was observed in Band 6, with one spectral window centered on the rest frequency of the CO(2-1) line at 230.5380000 GHz. Continuum was observed at frequencies of 228.5009 GHz, 213.5009 GHz, and 216.009 GHz. The CO spectral window was observed in a 1.875 GHz-wide band, divided into channels of 488.281 kHz (0.63 km s^{-1}). Continuum windows all had total bandwidths of 2 GHz and channel widths corresponding to 21.7 km s^{-1} .

During the 24-June-2015 observation the star underwent a bright flare for the last seven minutes of scheduling (Daley et al. in prep). Although unlikely to affect our

measurements of the molecular gas, out of caution we remove the last on-source integration time of 04:23:38-04:29:58 (UTC). However, comparisons of observations before and during the flare appear similar and uncompromised. Images produced from the three concatenated observation dates are shown as a set of channel maps in Figure 2.1. The seemingly random scattering of noise does not show a clear presence of signal located around the central star, shown as a black marker in each image. Additionally, Moment 0 and 1 maps (Figures 2.2(a) and (b), respectively) show no disk gas or velocity structure.

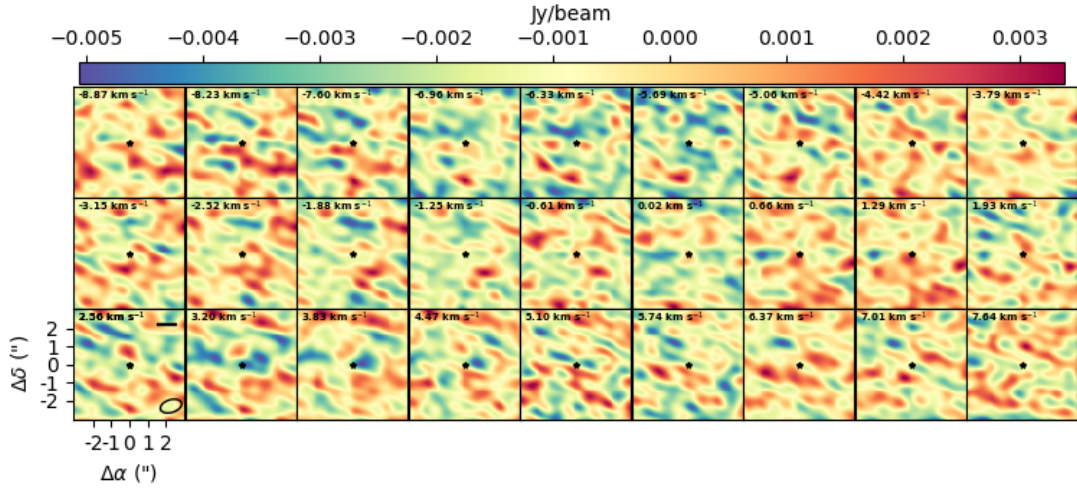


Figure 2.1: Velocity channel maps for AU Mic, showing flux density (Jy) per beam values per velocity space for CO(2-1). The lower left image shows the beam size (lower right hand corner), scale bar (upper right hand corner), and velocity channel (upper left hand corner). The scale bar represents 10 au. The beam size from the naturally weighted combined image is $1.22'' \times 0.71''$. The seemingly random scattering of noise shows no clear presence of gas, which one would be able to observe in the form of a ‘butterfly’ pattern (see 49 Ceti observations). The zero-point axes labels for RA and Dec refer to the pointing center of the observation, centered around the location of the star (shown as a small black star in the center of each channel).

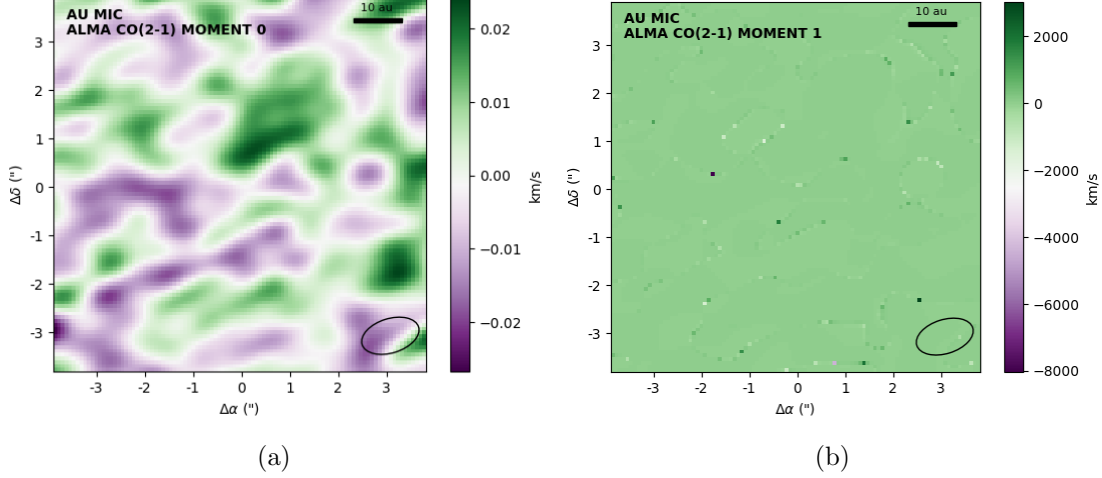


Figure 2.2: The Moment 0 and Moment 1 maps for AU Mic. The naturally weighted beam size is located in the bottom right, and a scale bar representing 10 au is in the upper right. The center of the images ($RA = 0$, $Dec = 0$) are the pointing centers of the observations located at the star. (a) The lack of any apparent disk structure indicates little-to-no gas presence. (b) As there is seemingly no disk structure in the Moment 0 map (a), there is likely no clear velocity field structure. Notice the large unit size on the colorbar, an artifact of a lack of signal and attributed to a few random pixels. The majority of pixels contain velocities within $\pm 20 \text{ km s}^{-1}$ of the star’s systemic velocity.

2.2 49 Ceti

We utilize previous observations of 49 Ceti in continuum, HCN(4-3), and CO(3-2) from 04-November-2013. In 40 minutes of on source time the CO(3-2) line and continuum are strongly detected with total integrated flux and flux density values of $6.0 \pm 0.1 \text{ Jy km s}^{-1}$ and $17 \pm 3 \text{ mJy}$, respectively (Hughes et al., 2017). These measurements agree with values obtained by Dent et al. (2005) and Meeus et al. (2012). The PWV values were constant through the observations with an average value of 0.37 mm. The 28 12-meter antennas range in baselines from 5-900 meters, configured to observe the CO(3-2) molecular transition at 345.7959899 GHz in Band 7 and the HCN(4-3) transition at 354.5054759 GHz. The CO window has a channel width of 61.04 kHz ($.0529 \text{ km s}^{-1}$) and a bandwidth of 234 MHz while the HCN window has a channel width of 488 kHz (0.413

km s^{-1}) and a bandwidth of 1.9 GHz. The narrow channel widths allow for a detailed characterization of the gas kinematics, centered around the star's systemic velocity of 2.78 km s^{-1} (Hughes et al., 2017). Additionally, the interferometer was configured to look in the continuum bands centered at 344 GHz and 357 GHz, each with bandwidth of 3 GHz and channel widths of 15.6 MHz. Channel maps for CO(3-2) and HCN(4-3) are shown in Figure 2.3, while Figure 2.4 depicts the Moment 0,1 maps for CO(3-2) and Moment 0 map for HCN(4-3).

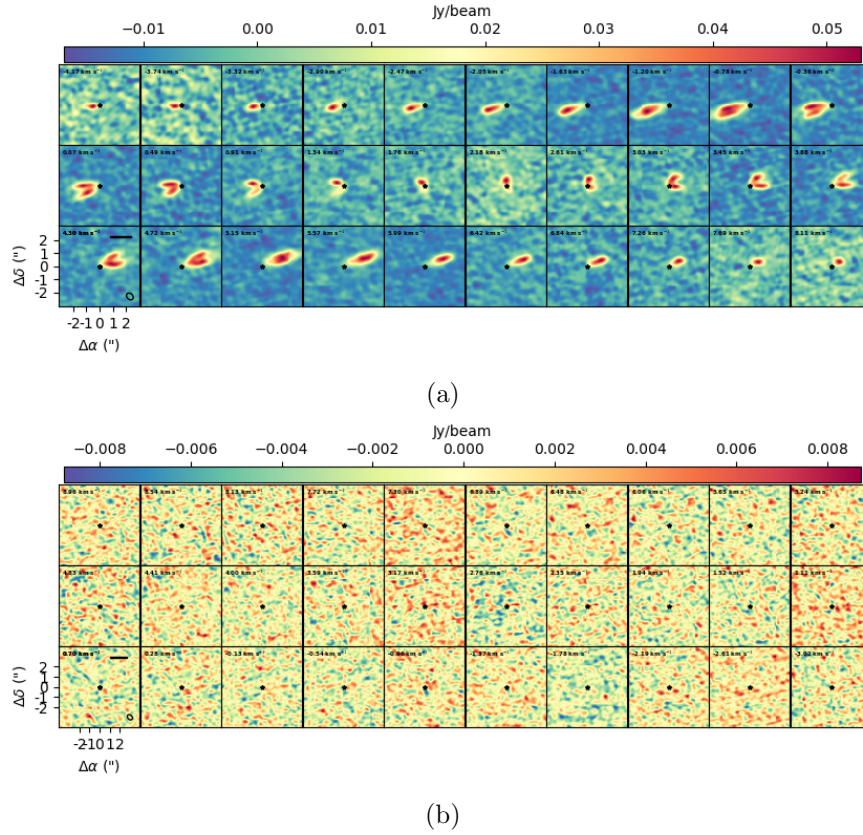


Figure 2.3: Velocity channel maps for 49 Ceti CO(3-2) (a) and HCN(4-3) (b), showing flux density (Jy) per beam values per velocity space. The lower left image shows the beam size (lower right hand corner) and scale bar (upper right hand corner). The scale bar represents 100 au. The black marker in the center of each channel represents the location of the star. The random scattering of noise and lack of a distinct butterfly pattern in the HCN maps (b), as compared to channel maps for CO (a), indicates that scarce amounts (if any) of HCN is present in the disk.

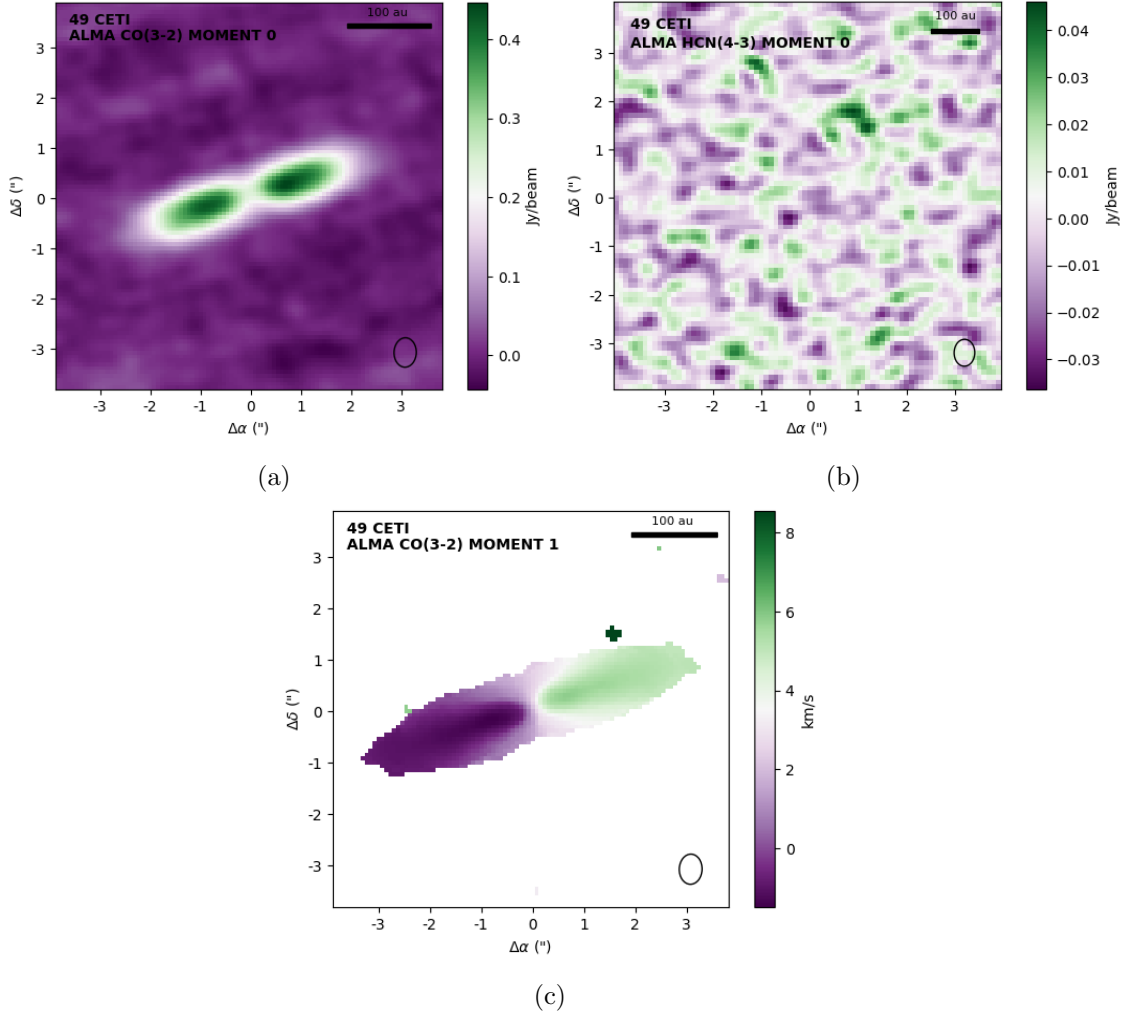


Figure 2.4: The Moment 0 maps for 49 Ceti (a) CO(3-2), (b) HCN(4-3), and (c) Moment 1 map of CO(3-2) for 49 Ceti. The naturally weighted beam size is located in the bottom right, and a scale bar representing 100 au is in the upper right. The center of the images ($RA = 0$, $Dec = 0$) are the pointing centers of the observations located at the star. (a) The beautiful disk structure shows a nice presence of gas equally distributed along both sides of the disk along the major axis (b) The lack of gas signal is quite evident here, similar to the Moment 0 map seen for AU Mic (Figure 2.2.a) (c) As there was clear disk structure for the Moment 0 map for CO(3-2), we are able to see the velocity field of the gas. Pay close attention to the units - as the star has a systemic velocity of 2.78 km s^{-1} all of the velocity values are shifted accordingly, explaining why the center of the disk does not have $V = 0 \text{ km s}^{-1}$.

CHAPTER 3

MODELS

*...through hard seas that shake and tremble I feel the surge
of progress, the slow rick-rocking of the horizon growing
and the constant creak of a beast beneath, outstretching
arms forward...*

The search for gas in debris disks has several inherent problems and challenges. As molecular gas lines from debris disks are very faint, often due to a low gas mass, the signal-to-noise ratios of the gas are also small. In order to make any detections or place sensitive limits it is thus necessary for us to maximize SNR in our models. Another challenge stems from the fact that line emission is spread out spatially and spectrally so that any given aperture contains a lot of noise coinciding with the signal. As we'd like to know the total gas emission across the entire disk the limitation of only looking at certain 'regions' presents observational issues that our models must take into account when determining an integrated flux.

We attempt to overcome these obstacles with two methods: first (Section 3.1), we will implement a basic spectral-domain modeling technique to integrate all possible channels containing line emission while comparing our observational data to expected line profiles for a Keplerian disk with matching parameters. Second (Section 3.2), we employ a more complex spectral-spatial shift method to maximize the SNR by minimiz-

ing the number of specific ‘noisy’ pixels in the data. This method builds off of the basic spectral model by taking into account the entire 3D position-position-velocity cube.

3.1 Keplerian Rotation Spectral Method

Here we undertake the creation of a simple geometrically-thin circumstellar debris disk in Keplerian rotation model using basic known stellar and disk parameters to simulate a Flux Density vs Velocity spectrum that we can compare with the entire observed spectrum as a matched filter to increase our sensitivity to faint integrated flux values. As the excitation of the emission line, as well as its status in LTE or not, is not specifically well known we neither assume that the disk is optically thick or optically thin. As we are fitting the flux profile and not the surface density this should not have a major effect on our model. Our model disk in Keplerian rotation assumes several basic stellar parameters, as well as a surface brightness power-law profile described in Equation 3.2. In addition to basic stellar parameters of mass (M_*), inclination (i), systemic velocity (V_{sys}), and distance (d), we also include previously determined parameters regarding the debris disk structure, such as integrated flux (F), power law (x), outer radius (r_{out}), inner radius (r_{in}), and position angle (PA). The stellar parameters are relatively well known values for our sources, and the disk parameters we take from recent work on the gas and/or dust disks. In the case of AU Mic, where there are no observations spatially constraining the gas disk, we must use disk parameters from dust continuum observations (MacGregor et al., 2013). Even though we don’t expect the gas disk to follow the same radial surface brightness profile of the dust disk, we generally assume that the radial extent is similar at the outer edges (Hughes et al., 2018). We thus use the dust disk as a starting point for a model that would be otherwise poorly constrained using an upper limit on the total gas flux. These parameters are listed in Table 3.1.

Parameter	49 Ceti	AU Mic
M_* (M_\odot)	2.1 ¹	0.31 ²
i ($^\circ$)	80 ³	90 ⁴
V_{sys} (km s^{-1})	2.78 ³	1.2 ⁵
d (pc)	59 ⁶	9.9 ⁶
F (Jy km s^{-1})	6.0 ³	0.07 ⁷
x_{pwr}	1.27 ³	2.32 ⁴
r_{in} (au)	20 ³	8 ⁴
r_{out} (au)	220 ³	40 ⁴
PA ($^\circ$)	-71 ³	128 ⁴

1: Roberge et al. (2013), 2: Plavchan et al. (2009), 3: Hughes et al. (2017),
4: MacGregor et al. (2013), 5: Duflot et al. (1995), 6: van Leeuwen (2007), 7: This Work

Table 3.1: Free parameters for our two sources, AU Mic and 49 Ceti. The line break in the middle separates the stellar parameters (above) and the disk parameters (below). Superscripts indicate the source, which is listed at the bottom.

From these basic parameters and Keplerian laws of rotation, we construct a position-position image of pixel space similar to our actual data. In this case, the image contained 240×240 pixels, each with a corresponding velocity value calculated from Kepler's laws and scaled based on the inclination of the disk. We use a pixel size corresponding to ~ 0.1 arcseconds after factoring in the wavelength of our observations, the maximum beam size, and the diameter of the antennas. As a result, each pixel is small enough to represent a fraction of the synthesized beam size. Equation 3.1 below gives us our scaled velocity values at each pixel (x,y).

$$V(x, y) = \frac{GM_*}{\sqrt{x^2 + y^2}} \sin(i) \cos(\arctan(\frac{y}{x})) + V_{sys} \quad (3.1)$$

where (x,y) is the individual pixel location and $\sqrt{x^2 + y^2}$ is the vector distance from the star to the pixel. Figure 3.1 shows us the visual representation of the velocities, with color indicating different velocities. Negative and positive values correspond to blueshift and redshift, respectively. The star's systemic velocity is added to each calculated

velocity to adjust for the radial motion of the system. The disk in Figure 3.1.b appears flattened due to the disk's inclination to the viewer's line of sight (LOS).

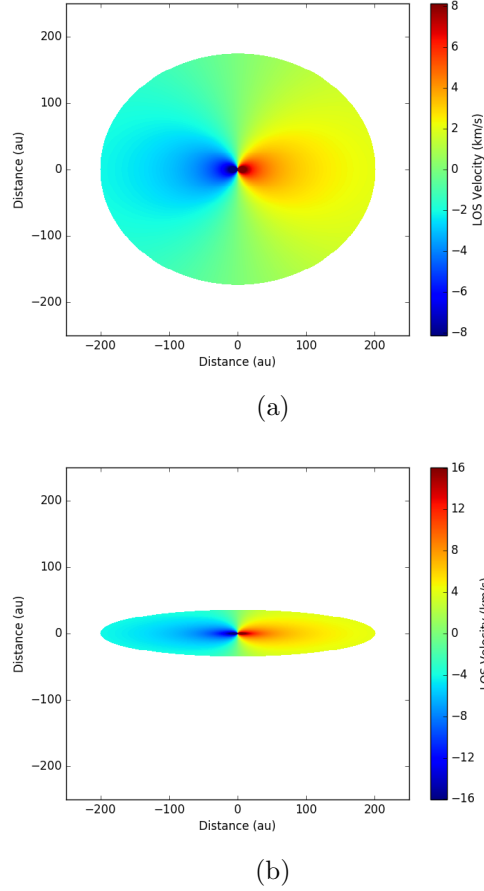


Figure 3.1: Keplerian velocity fields calculated for geometrically thin disks viewed at different inclination angles. (a) shows an example of a nearly face-on disk ($i = 30^\circ$), while the (b) shows an example of a disk viewed close to edge-on ($i = 80^\circ$).

We are now able to break down these values into smaller velocity ranges, called ‘channels.’ Each channel is defined by a range of velocities that includes all pixels and emission found within said velocity range. Thus we are able to obtain (x,y) pixel locations for all pixels with a given range of velocity values. Splitting out a specific range of velocities gives us cut-out image of the previous velocity models (Figure 3.1), as seen in Figure 3.2.

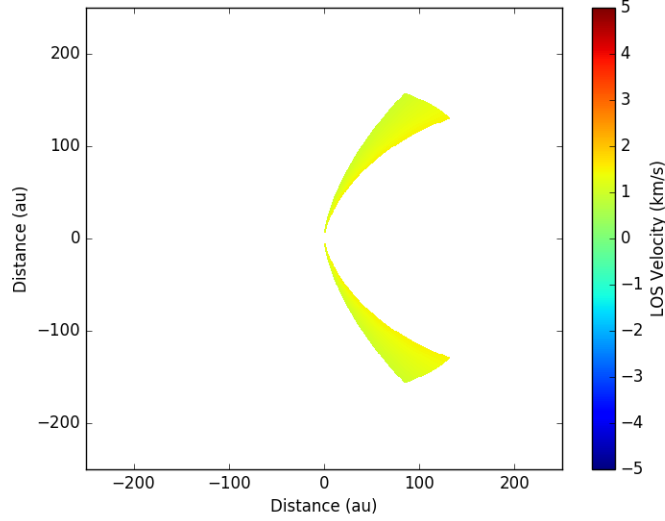


Figure 3.2: Keplerian velocity fields from for a single channel, with LOS velocities between $1 - 1.5 \text{ km s}^{-1}$. The disk parameters are the same as those of Figure 3.1.a, with an inclination of $i = 30^\circ$. Notice that this model is the same butterfly pattern seen in channel maps with large amounts of signal.

From these velocities, we now calculate and overlay additional flux density values at a deprojected distance R from the star and based on a surface brightness power law profile, detailed in Equation 3.2.

$$F(R) = F_o R^{-p}$$

$$F_{tot} = \int_{R_{in}}^{R_{out}} F(R) 2\pi R dR \quad (3.2)$$

where p is the power law index (x_{pwr} in Table 3.1), often used as a free parameter. Visually the flux density profile appears in Figure 3.3, where a hard outer disk radius is used to limit measurements of the flux density surface brightness profile to where $R < 200 \text{ au}$ from the star. We are able to overlay the (x,y) pixel locations obtained from a select range of velocities (Figure 3.2) to obtain a range of flux values per velocity range (Figure 3.3). We obtain flux values for every velocity range throughout the disk, providing a flux density vs velocity spectrum plot, Figure 3.4.

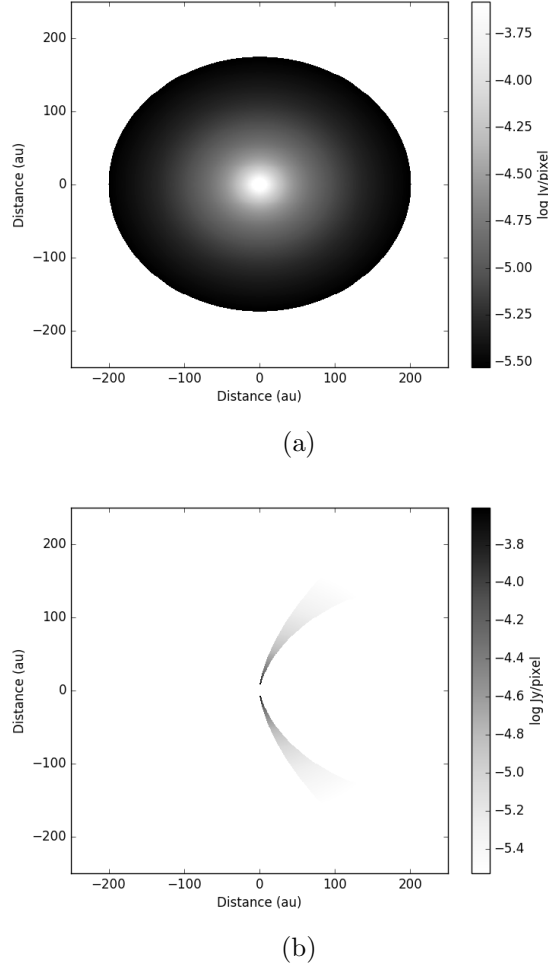


Figure 3.3: (a) The log flux density power-law brightness profile for a debris disk with the same parameters as Figure 3.1.a and 3.2, with $i = 30^\circ$. A power-law of $x_{pwr} = 1.5$ was used for this specific model. We restrict our model to a radius of < 200 au from the star, or central pixel. (b) The log flux density power-law brightness profile for a single velocity channel of $1 - 1.5 \text{ km s}^{-1}$ for a debris disk with the same parameters as (a).

From observations we are able to construct similar flux density vs velocity spectrum plots as in Figure 3.4, thus allowing us to compare our model to actual data. For statistical comparisons we use a χ^2 metric, to quantify the goodness of fit between the model and the data. We calculate χ^2 using Equation 3.3 below.

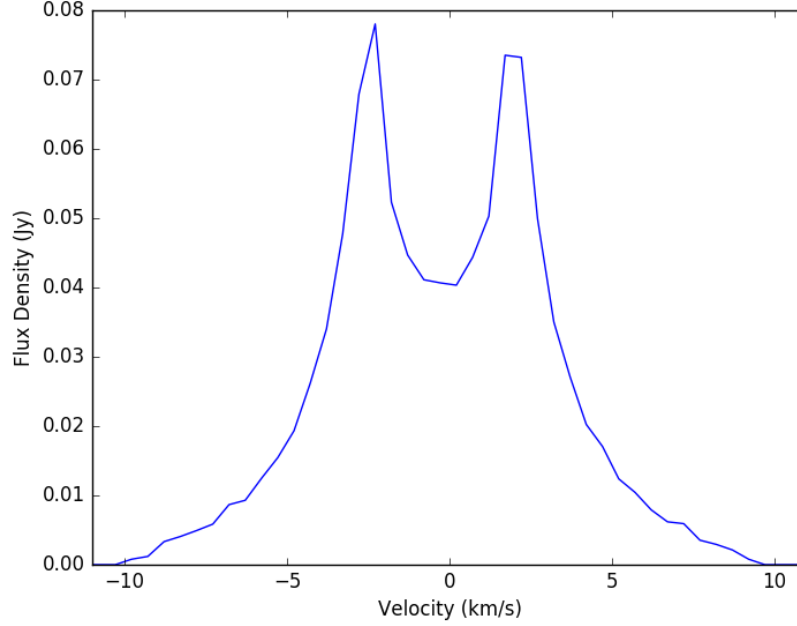


Figure 3.4: Flux density vs velocities for a most basic stellar debris disk model using the Keplerian velocity fields from Figure 3.1(left panel) and the power-law flux brightness profile from Figure 3.3.a. Integrating flux per velocity channels, as seen in Figure 3.3.b, provides integrated flux density values for each 0.5 km s^{-1} channel of velocities. The ‘double peak’ structure with a local minimum at 0 km s^{-1} signifies the blue and redshift portions of the disk.

$$\chi^2 = \sum_{i=1}^n \frac{(data_i - model_i)^2}{\sigma^2} \quad (3.3)$$

where $data_i, model_i$ are corresponding flux density values found within the same velocity channel and σ is the RMS of the data. A small χ^2 value is the goal, as it represents the set of model parameters that best reproduces the features found in the data.

In order to accurately compare the model and data, the velocity grids must be precisely aligned. We generate each model velocity grid based on the channel velocities

and widths of the data. The location of the model velocity field depends wholly on the pixel location of the star in the data and the position angle of the disk. We assume from our observations that the pointing center is the location of the star unless otherwise determined, while the PA we obtain from previous studies regarding dust, and gas if possible, in the disk. Even slight variations (< 2 pixels) between the model and data grids show a major impact on the total flux value.

Our Keplerian spectral model involves several free parameters discussed earlier in the section (and listed in Table 3.1). We adjust the integrated flux parameter value for comparison of our model spectrum to the data spectrum, producing a χ^2 value for each model. A basic grid search function is utilized to find the optimal constraints on our free parameters by stepping through a range of free parameters and locating the minimum χ^2 value, corresponding to the best model and therefore the most likely free parameter values.

In a well characterized source like 49 Ceti, for which the inclination, position angle, and power law flux dependence are known from previous CO observations (Hughes et al., 2017), we can fix the known disk geometry and vary only the total flux of the HCN line. For AU Mic, no previous molecular line emission has been detected, but the dust continuum constrains some disk parameters like inclination and position angle (MacGregor et al., 2013). While re-emphasizing our assumption (and its limitations) that the dust and gas spatial distributions are the same, utilizing parameters from preceding observations, which place better constraints on disk parameters, allows us in turn to place a better limit on the total flux.

Finally, if our model and data indicate that there is no apparent gas detection then we are able to place a 3σ upper limit on the total flux. We assume a standard χ^2 likelihood function and calculate a probability interval for its correspondence to a Gaussian standard deviation. Equation 3.4 details the process, where according to Gaussian distributions and the 68 – 95 – 99.7 rule on standard deviations the 3σ value for a χ^2 distribution constrains a probability interval of 99.7% of terms. As the $\chi^2_{3\sigma}$

value is dependent on the χ^2_{min} value, this probability interval, equal to $1 - 99.7\%$, represents the $\Delta\chi^2$ value. As our 3σ total flux value corresponds to the $\chi^2_{3\sigma}$ value, we must calculate $\Delta\chi^2$ to determine $\chi^2_{3\sigma}$, and thus, $F_{3\sigma}$. Figure 3.5 shows the relationship between total flux and its corresponding χ^2 values. The blue line shows the χ^2 and total flux relationships, while the dashed red line shows the total flux value where the χ^2 value is at the 3σ standard deviation.

$$\begin{aligned}
 e^{\Delta\chi^2/2} &= 0.3\% \\
 \chi^2_{3\sigma} &= \chi^2_{min} + \Delta\chi^2 \\
 F_{3\sigma} &= F(\chi^2_{3\sigma})
 \end{aligned} \tag{3.4}$$

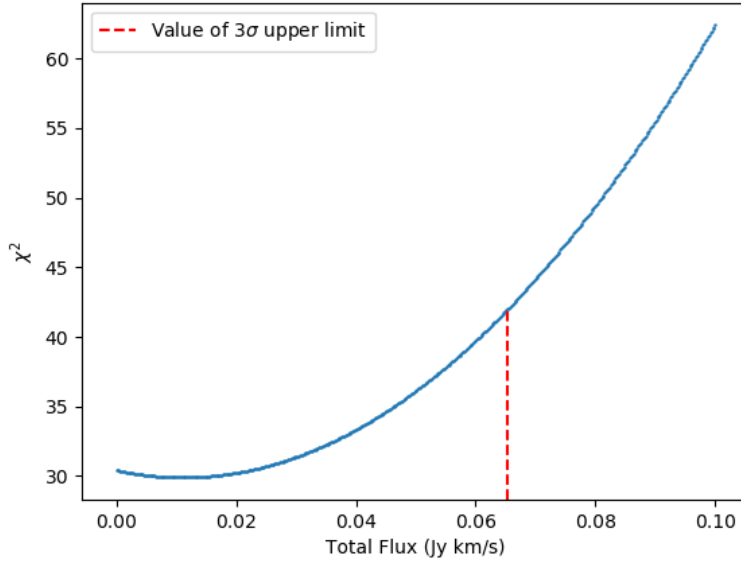


Figure 3.5: χ^2 value as a function of integrated flux for the AU Mic observations of CO(2-1). The χ^2 values increase from the minimum value at a flux of 0.0 Jy km s^{-1} (blue line), and the $\Delta\chi^2$ difference at $\sim 0.07 \text{ Jy km s}^{-1}$ corresponds to a 3-sigma upper limit on the flux (red dashed line).

3.2 Spectral Spatial Shift

While the Keplerian-spectral model works quite well in accurately judging upper limits on gas in disks, Matr  et al. (2017b) shows that it is possible to obtain even more sensitive upper limits when accounting for spatial/velocity distributions to maximize SNR. As most debris disks, both currently surveyed and in theory, contain a limited-to-no gas presence, it is vital place sensitive limits on the amount of gas in the system. The problem arises from the structure of the model in its attempt to directly replicate data spectra. In a disk with a heavy and clear presence of molecular gas the spectra appears as a well defined (and positive) double peak. However, when there is no obvious gas detection, the data spectrum can dip down both into the negative flux density axis, as well as the positive. The negative dip is typically due to random noise in the data affecting the spectrum. However, as the disk is in Keplerian rotation we are able to determine where signal should be, thus allowing us to remove pixels where only noise is expected and in so doing drastically raise our SNR.

We utilize this method developed by Matr  et al. (2017b) to increase our signal-to-noise (SNR) and thus overcome problems with “no-detection” scenarios. This spectral-spatial shift model builds on the same velocity field foundation as our Keplerian spectral fitting model, but rather applies them differently to reduce the noise.

The method takes into account the same basic stellar parameters discussed in Section 3.1 to build the $V(x,y)$ velocity field at a pixel and distance scale (Figure 3.1) similar to the data visibility images. We begin with reduced ALMA channel maps of spectral line data and shift the spectrum associated with every pixel to place the channel with the strongest expected emission at a velocity of zero. The data channel maps exist as a position-position-velocity data image cube, with each pixel in the $(240, 240, n)$ grid containing flux information for its location on the sky, where n is the number of channels. A typical spectrum for a single pixel containing a non-zero amount of gas is shown in Figure 3.6 below. The spectrum is taken from observations of CO(3-2) emission in 49 Ceti presented by Hughes et al. (2017), which we used to test the spectral-spatial shifting

method on before applying it to observations where no signal was clearly detected. Note the large single spike, indicating the velocity location of the max amount of signal. The smaller peaks along the bottom, all around 0 Jy, indicate random noise in the pixel at far off velocities.

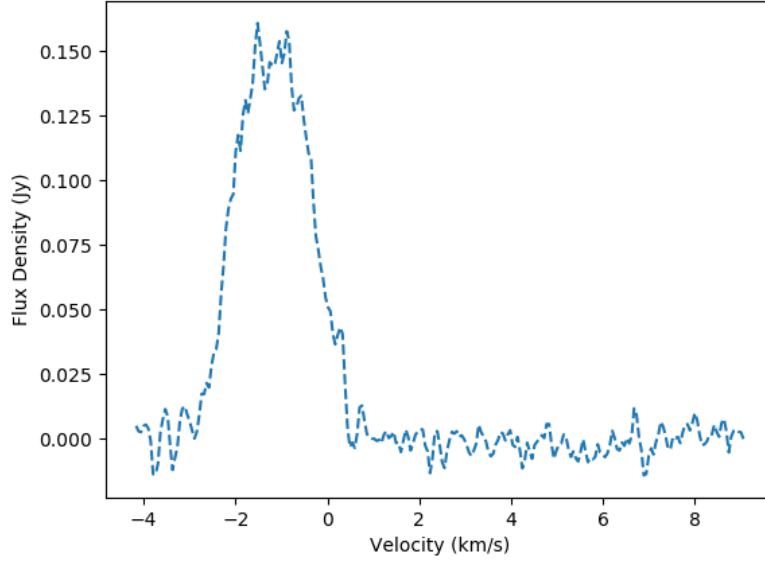


Figure 3.6: Spectrum of CO(3-2) emission from the disk around 49 Ceti for a single pixel at a position offset of (0.32,1.68) arcsec relative to the disk center.

We determine the theoretical Keplerian velocity at this specific pixel’s location from Figure 3.1, and then we ‘shift’ over the spectrum by that velocity value. This can easily be done by subtracting the theoretical velocity from the spectrum’s x-axis velocities, and then interpolating the spectrum to fill in a new velocity grid. Figure 3.7 shows the spectrum for a single pixel before and after we apply the shift, while Figure 3.8 shows the shift of 40 random pixels using known velocities from the CO(3-2) detection. The shift aims to move the peak of the spectrum to the central channel, which is at the mercy of the user, but we chose $V = 0 \text{ km s}^{-1}$. We apply this shift to every pixel in the 3D image cube to obtain a new image cube of the same parameters. The importance of shifting

multiple pixels correctly stems from the necessity to match up the corresponding pixels between the Keplerian velocity model and the data images, as we have covered in our previous method. But above pixel location matching, the one major concern with this method is its total dependence on the precision of the theoretical velocity field.

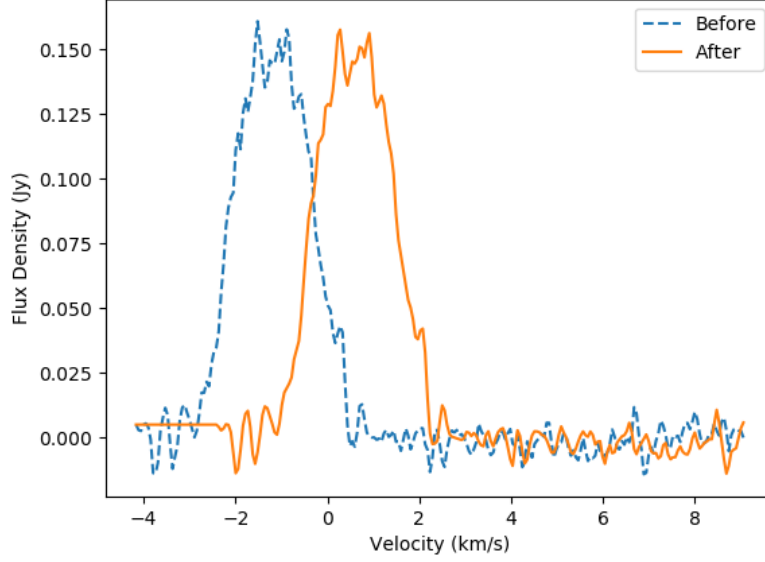


Figure 3.7: Spectrum of CO(3-2) emission from the disk around 49 Ceti for a single pixel at a position offset of (0.32,1.68) arcsec relative to the disk center. This spectrum illustrates the predictable velocity offset of the emission from the systemic velocity of the source, due to the Keplerian rotation of the disk around the star. The spectral shift method applies an offset along the velocity axis to shift the emission in every pixel into the zero-velocity channel, in order to concentrate the signal and thereby maximize the SNR of the data. The spectrum after the shift (orange line) is not quite located at the desired velocity of $V = 0 \text{ km s}^{-1}$ due to the lack of precision between the Keplerian model velocity field and the velocity field of the data.

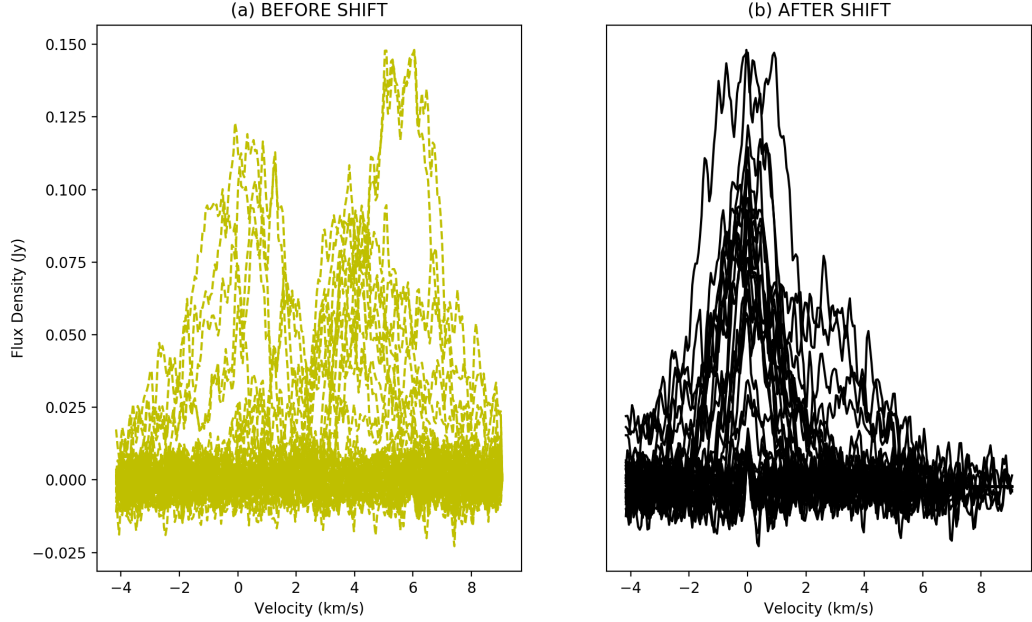


Figure 3.8: Spectrum of CO(3-2) emission from the disk around 49 Ceti, both before (a) and after (b) a spectral-spatial shift is applied. The spectrum showcase the ability of the model to shift multiple pixels by corresponding velocity field values in the same method as Figure 3.8. The shift is applied to spectrum for 40 random pixels at position offsets of $0 - 0.4$ and $1.6 - 2.0$ arcsec relative to the disk center using known velocities from CO(3-2) detections. Pixels are shifted to a single channel with a velocity of 0 km s^{-1} .

We test the code by applying the shift method to the 49 Ceti CO(3-2) data, which exhibits high SNR. Figure 3.9 shows the effect of the shift on the data channel maps, both before (a) and after (b). Our un-altered channel maps indicate the presence of gas throughout a well displayed butterfly channel map pattern. Each channel shows emission on only one side of the star position, due to the red and blue shifts from the rotating disk. After we apply the shift, however, the bulk of signal is moved to the the three channels located roughly at $V = 0 \text{ km s}^{-1}$, ranging from $V = -0.75 \text{ km s}^{-1}$ to $V = 0.30 \text{ km s}^{-1}$. Thus we are able to see that our shift correctly re-located the data to the desired channel(s). The difference between this method and our previous

double peak method is abundantly obvious in the SNR statistics, with an increase in SNR by a factor of 2. This increase is due to our ability to concentrate more of the signal in the central channels while moving more of the noise to other velocities, thereby increasing the SNR of the line measurement when using only the data close to a velocity of zero. When normally calculating the integrated flux in our Keplerian rotation spectral method, all pixels over all velocity channels are added together in the position-position-velocity cube. This results in the addition of both signal and noise together. However, in our shift model, we are re-locating only the velocity planes of each pixel that *should* have signal, and are thus dispersing the rest of the velocity channels containing random noise. The end result is a smaller number of channels containing the majority of signal. This smaller number of channels does still have some noise, which we attempt to overcome by restricting the flux integration to the spatial region covered by the disk, or the disk's outer radius.

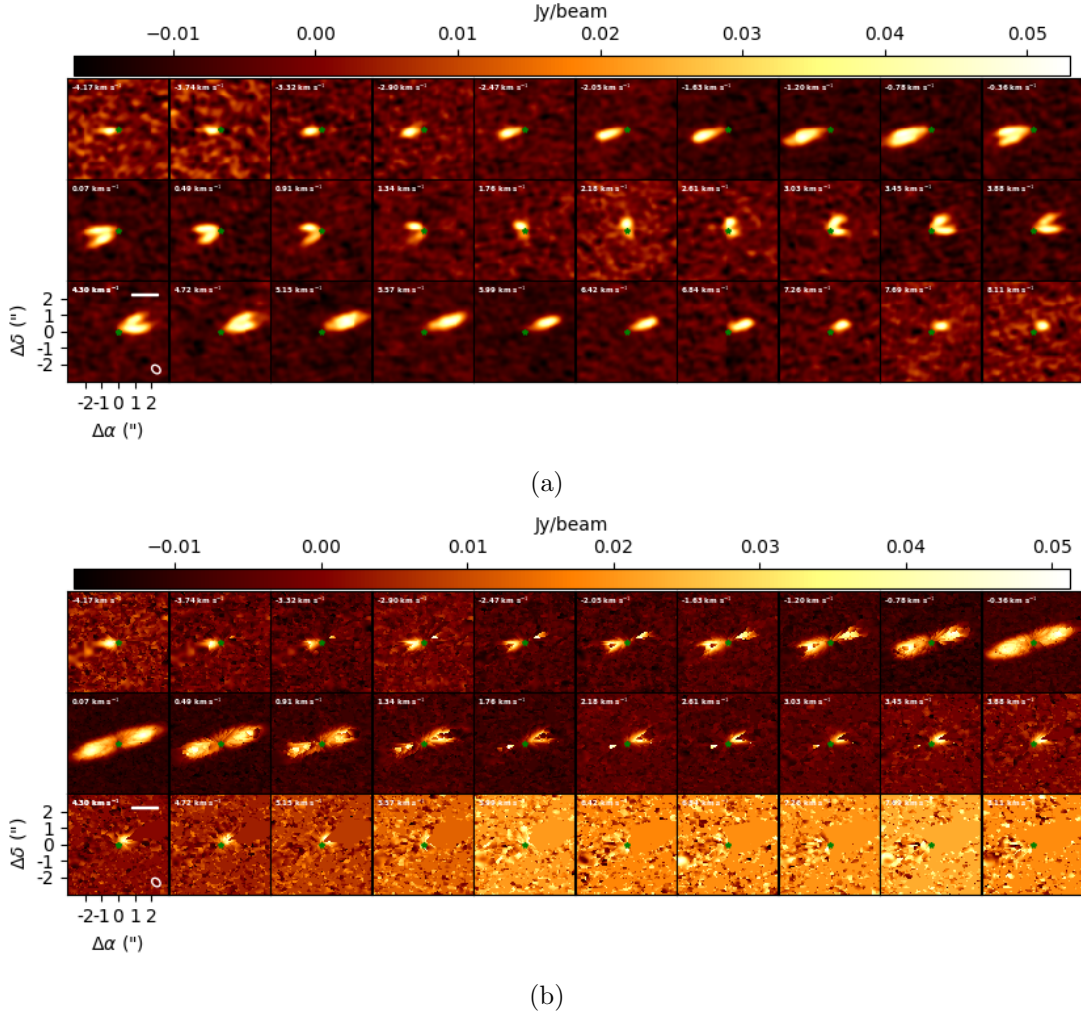


Figure 3.9: Velocity channel maps for 49 Ceti CO(3-2) both before (a) and after (b) a spectral shift method was applied to the data, shown as flux density (Jy) per beam values per velocity space. The lower left image shows the beam size (lower right hand corner) and scale bar (upper right hand corner). The scale bar represents 100 au. The bright ‘butterfly’ pattern in (a) is integrated together into only a few channels in (b) located around $V = 0 \text{ km s}^{-1}$. The effectiveness of the method is seen both in these two panels as well as in the fringe panels, which showcase large amounts of random scattered noise. The star’s location is shown by the green marker, perfectly at the center of emission.

3.2.1 Velocity Maps

In the interest of gaining the highest SNR possible, we compare several different velocity fields to use in our shift. With previous knowledge of the source’s velocity field, such as in 49 Ceti, it is feasible to use any of three different velocity fields: a Keplerian model, a moment 1 model, and the velocity corresponding to the maximum flux in the spectrum of each pixel from the 3D channel maps. In the case that there are neither interferometric gas detections nor knowledge of the source’s velocity field from observations, as for our AU Mic data, it is only possible to use the Keplerian model.

To achieve a perfect shift of the pixel’s spectrum back to the central velocity channel, the velocity that it is shifted by must be as precise to the velocity intercept of the spectrum peak as possible. Only a perfect velocity match will correctly shift the peak of the spectrum to exactly $V = 0 \text{ km s}^{-1}$ or $V = V_{sys}$. Slight deviations in this precision shift the peak signal to just off center, resulting in a widened or dispersed central peak with lesser SNR. Thus, a velocity field that closely matches the actual velocity field of the source results in an increase in SNR, which, in turn, results in an increase in sensitivity on placing upper limits or detections.

Our test data, 49 Ceti CO(3-2), contains vividly apparent signal in the channel maps. We can also use it to generate a moment 1 map based solely on the data. To test the effect of different velocity fields, we apply our spectral spatial shift model to the 49 Ceti CO(3-2) data using three separate velocity fields, shown in Figure 3.10. The three fields are our standard Keplerian rotation model used throughout all of our models (left panel), the moment 1 velocity map taken from the data (right panel), and velocity locations of the max flux signal peak in each pixel spectrum (middle panel). The latter determines its velocities directly from the pixel spectrums, allowing for the most accurate possible velocity, as it is taken from the signal itself. Naturally this, plus the moment 1 map, are not feasible options for disks that do not contain overly-apparent signal in their data, however they do show the merits and effects of utilizing information from known CO velocity fields to increase sensitivity of faint molecular species at lower

abundance. The single contours indicate V_{sys} of the source, correctly located in the stellar location. We must point out the noticeable differences between the Keplerian model (left panel) and the true velocity fields from CO detections (middle, right panels). We suspect the difference is due to radiative transfer effects in optically thick gas or possible slight deviations from true Keplerian rotation within the disk. The application of the different velocity fields yields the following shifted spectrum (Figure 3.11) and statistical results (Table 3.2).

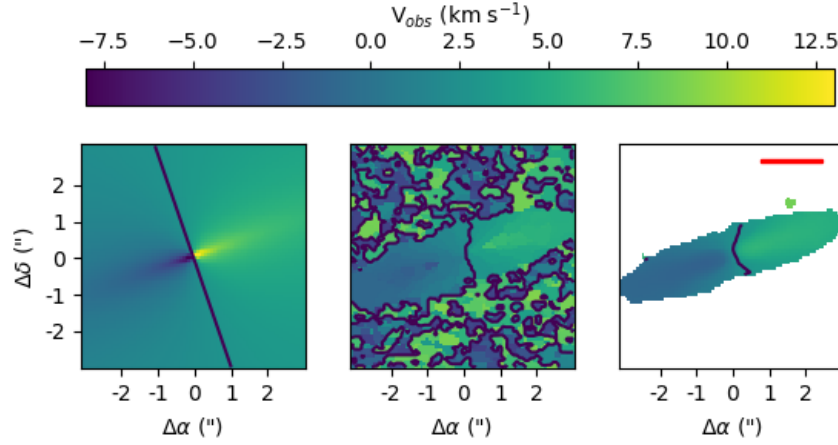


Figure 3.10: Varying velocity fields for 49 Ceti with a single contour line at the systemic velocity of $V_{sys} = 2.78 \text{ km s}^{-1}$ (Hughes et al., 2017). The left panel shows a velocity field created using simple Keplerian rotation with a disk inclination and position angle; the central panel's velocity field is obtained using the velocity locations of the max flux signal peak in each pixel spectrum; the right panel's velocity field is from a standard Moment 1 map (intensity-weighted coordinate velocity fields). The scale bar in the top right hand corner of the right panel represents 100 au. Notice that the single contour lines of the systemic velocity lie almost directly along the semi-minor axis of the disk, as expected.

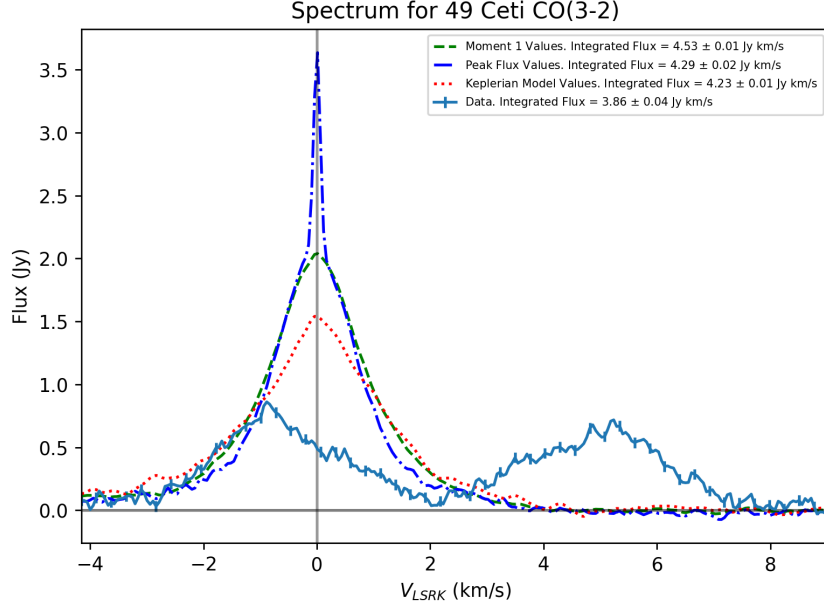


Figure 3.11: Molecular line spectral flux shifting for 49 Ceti CO(3-2) by velocity source: Moment 1 map (green dashed), Peak known CO(3-2) (blue dashed), Keplerian model (red dashed), plus the un-altered spectrum from the original data (solid blue). Notice the varying widths and peaks of the different velocity methods, with a higher peak and minimal line spreading corresponding to a larger SNR.

Shift Velocity Field	SNR
Peak Spectrum Flux	127
Moment 1	71
Keplerian Model	54
Keplerian spectral fitting model (<i>Non shift method</i>)	30

Table 3.2: The SNR statistics for the central channels (peaks) in Figure 3.11 based on the different velocity fields used. As expected from Figure 3.11, a larger certainty and precision in velocity field values directly relates to a higher SNR. Moreover, we effectively show that the inclusion of spatial/velocity distributions directly affects the SNR and sensitivity of total integrated flux measurements.

As we can see both visually in Figure 3.11 and also in Table 3.2, using the velocities from the actual data spectrum produces the best SNR, with the moment 1 map also providing a better SNR and peak than the standard Keplerian rotational model. The results also indicate the superiority of the spectral-spatial method in general over our Keplerian spectral fitting method. As we know that the SNR *can* be drastically increased, it falls on us to determine a better course of action to create a more complex velocity map that can handle an increase in velocity sensitivity per pixel. Some current limitations with the Keplerian velocity field are inherent in the resolution of the observations and the effect of convolution with the synthesized beam, which we do not include in our model. As such, with our current resolution the velocity gradient across pixels is simply not fine enough. For example, a pixel in the midplane of the disk may be several au from edge to edge and thus can individually contain several different velocity values. The current model does not have the ability to factor in this small of a gradient change, and instead only values in a single velocity for the entirety of the pixel. This is difficult to currently fix though, as the models necessitate matching pixel size and amount with the data. Attempts were made to convolve the image in CASA to try to simulate the effects of Keplerian shear on the model velocities. However, the convolved image and model appeared without marked difference from our original attempts, leaving us to conclude that observations with higher angular resolution are necessary to further increase the accuracy of the velocity field.

3.2.2 Velocity Maps of Edge-On Disks ($i \approx 90^\circ$)

As covered in Section 1.2.2, due to the scarce amount of gas present in debris disks it is often ideal to observe disks that lie perfectly edge on to the viewer to maximize the total integrated flux. With our basic Keplerian spectral model though, it is essentially impossible to set the inclination at $i = 90^\circ$, as limited velocity information would be returned detailing the vertical extent of the gas and the encompassing emission smeared out over multiple pixels by the beam. At high inclinations the flat Keplerian model

squishes down the disk to achieve the correct inclination, thus reducing the height of the disk from what we observe. Figure 3.12.a shows the effect of this ‘squish’ on the disk, where the real CO disk is observed to extend at least twice as far vertically as the model. Thus, pixels above and below the center midplane of the disk would have reduced velocities according to the model, but in reality they would have very similar velocities. Additionally, the data are convolved with the synthesized beam resulting in flux from the midplane leaching into nearby pixels above and below the midplane, something not currently accounted for by our flat Keplerian models. There is also the concern of different velocities mixing together along a particular line of sight in an edge-on disk, an inherent limitation in our ability to correctly shift the velocity field of an edge-on disk.

An attempt to counteract the problems of a flat Keplerian model involved the creation of a linear velocity field, in which pixel velocities were determined based on a simple linear scale from the midplane. Along the midplane of the disk velocities were calculated using Equation 3.5, and then these velocities were applied to all pixels on the same vertical axis, thus ensuring that pixels above and below the midplane were not subject to reduced velocities. For our calculation of V_{linear} only the distance along the major axis (x) was used, the minor axis (y) was ignored. Figure 3.12.b shows the linear velocity field after a PA was applied. The linear velocities produced a similar result to our other methods, confirming our other results of a lack of signal.

$$V_{linear}(x, y) = \sqrt{\frac{GM_{star}}{x}} + V_{systemic} \quad (3.5)$$

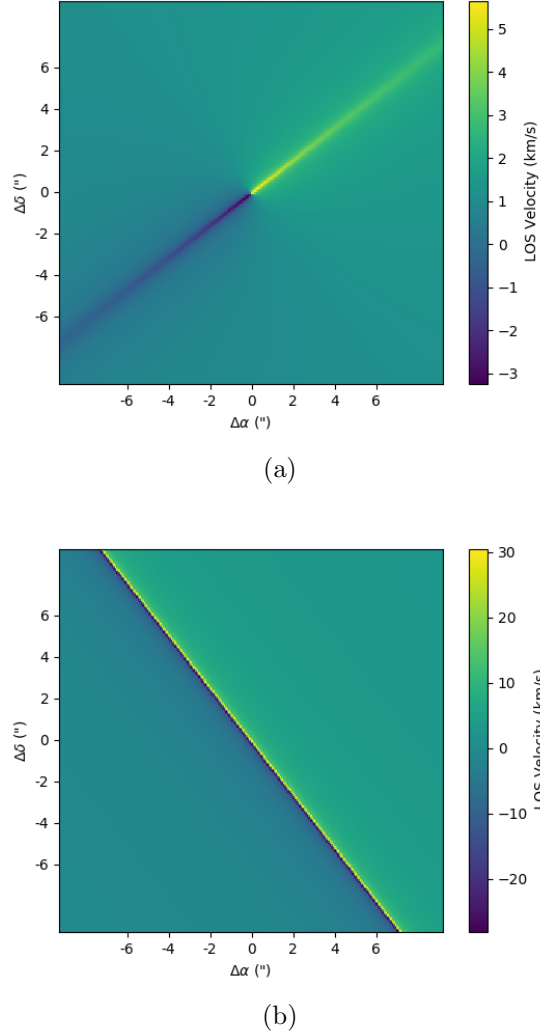


Figure 3.12: (a) Standard Keplerian velocity field of a close-to edge-on ($i = 89^\circ$) debris disk. We see that the disk is flattened dramatically at higher inclinations, which would be unable to accurately describe the velocity vectors of any gas in a puffy edge-on disk. (b) Keplerian velocity field of a close-to edge-on ($i = 89^\circ$) debris disk using linear velocities away from a single semi-major axis and ignoring the minor axis. In an edge-on disk it is hoped that a linear velocity field would be better suited to detail gas velocities above and below the midplane of the disk, thus accounting for the ‘puffiness.’ Unfortunately, as AU Mic shows no detectable signal we are only currently able to show that the linear velocity field produces the same upper limit as a standard Keplerian rotation field.

CHAPTER 4

RESULTS

*...toes deep in the heart of an unknown world speaks of
inspiration and bold frontiers courage. Yet here I remain,
bedrock un-quaked, listening to but a whisper in the wind's
change, perhaps to where I once was...perhaps to where I
will never be...*

4.1 Total Flux

4.1.1 AU Mic CO(2-1)

Cursory analysis of AU Mic CO(2-1) unprocessed channel maps and spectrum do not exhibit any statistically significant CO(2-1) emission. The raw spectra, shown as the green line in the Figure 4.1, is compared to spectrum that have been processed using the spectral-spatial shift method. As we have no previous velocity field knowledge for AU Mic gas kinematics it is necessary to apply two spectral-spatial shifts, accounting for different rotation orientations of the disk. We alter the orientation of our standard Keplerian velocity field by testing both the position angle constrained by MacGregor et al. (2013) at 128° and a rotation of this position angle by 180° . The blue spectrum shows a processed spectrum assuming the NW corner of the disk is blueshifted towards

the viewer. The red spectrum assumes the NW corner is redshifted away from us. Even after using the spatial-spectral shift method to increase the SNR there is no obvious detection of CO(2-1) emission with either rotational orientation of the disk. We thus place a 3σ upper limit on the integrated flux at $0.07 \text{ Jy km s}^{-1}$ with no specific preference to rotation orientation of the disk. While we obtain 3σ upper limits with our Keplerian spectral method using χ^2 statistical significance (Section 3.1), our limit of $0.07 \text{ Jy km s}^{-1}$ above was calculated as three times the standard deviation of our spectra after applying a spatial-spectrum shift method. Due to the uncertainty of the disk velocity orientation, we calculate 3σ limits for both shifted spectrums and average their values.

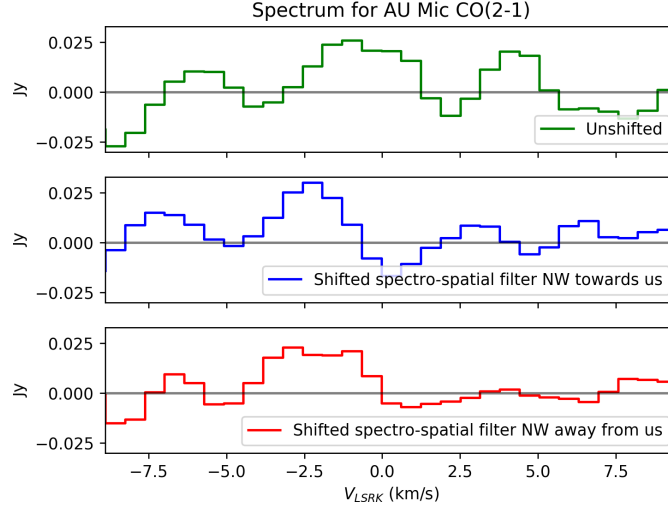


Figure 4.1: Spectrum of AU Mic CO(2-1) from an 8×8 arcsecond box centered at the pointing center of our observations: un-altered (green), using the spatial-spectral shifting method assuming the NW corner is blueshifted towards us (blue), and using the spatial-shifted method assuming the NW corner is redshifted away from us (red). Signs of a detection would show up as a peak in the shifted spectrum (blue or red line) located at $V_{LSRK} = 0$, similar to the central peaks in Figure 3.11. The lack of this central peak, in addition to random peaks and valleys indicates no detectable signal.

4.1.2 49 Ceti HCN(4-3)

Similar to our results for CO(2-1) in AU Mic we did not detect HCN(4-3) gas in our unprocessed observations. We applied the same spectral-spatial shift method to the data using the velocity field from the CO(3-2) Moment 1 map to shift the raw spectrum. As the disk rotation direction is well documented in 49 Ceti from CO(3-2) detections by Hughes et al. (2017) to be redshifted in the NE corner of the disk, it was not necessary for us to account for both directions as in the case of AU Mic. Figure 4.2 shows the spectrum for HCN(4-3), both before (green line) and after (blue line) the shift. It is obvious from the lack of central peak similar in the shifted spectrum to those seen in Figure 3.11 that there is no HCN detection. We place a 3σ upper limit on the integrated flux at $0.09 \text{ Jy km s}^{-1}$ in the same manner as for AU Mic.

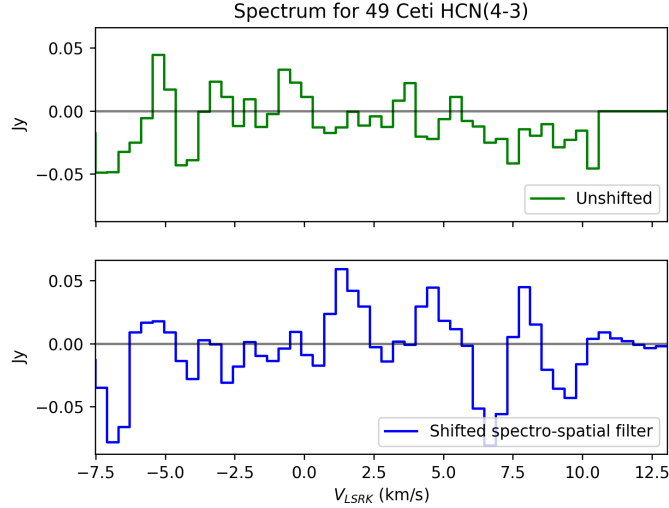


Figure 4.2: Spectrum of HCN(4-3) from an 8×8 arcsecond box centered at the pointing center of our observations: un-altered (green), altered with a spectral flux shifting method (blue). We only apply a single shift as we have velocity fields from previous detections of CO indicating that the NE side of the disk is redshifted away from us. Signs of a detection would appear as a peak in the shifted spectrum (blue or red line) located at $V_{LSRK} = 0$, similar to the central peaks in Figure 3.11.

4.2 Gas Mass

We use Equation 4.1 and the parameters in Table 4.1 to calculate an upper limit on the total gas mass in our two systems, where $F_{J_u-J_l}$ is our total flux upper limit, m is the mass of the specific molecule, d is the distance to the star, ν_0 is the rest frequency of the line, $A_{J_u-J_l}$ is the Einstein Coefficient of the line transition. The Einstein coefficient is the probability of the molecule spontaneously transitioning to the next lowest energy state per second. X_u represents the fraction of molecules populating the upper energy level (J_u) of the transition, which factors in the molecular rotational constant (B_0) and the excitation temperature (T_{ex}). The rotational constant describes the rotational energy state of the molecule with a dipole moment based on its inertia, while the excitation temperature is representative of the temperature allowing for a specific ratio of particle populations in the upper state (J_u) to the total molecular population. The determination of T_{ex} is thus dependent on multiple observational measurements to determine both upper state and total molecular populations. Other constants are involved in this calculation, such as Planck's constant (h), Boltzmann's constant (k), and the speed of light (c).

$$M = \frac{4\pi}{h\nu_0} \frac{F_{J_u-J_l} m_{molecule} d^2}{A_{J_u-J_l} X_u} \quad (4.1)$$

$$X_u = (2J_u + 1) \frac{e^{\frac{-B_0 J_u(J_u+1)hc}{kT_{ex}}}}{\frac{kT_{ex}}{hcB_0}}$$

4.2.1 AU Mic CO(2-1)

Parameter	Value	Parameter	Value
ν_0 (GHz)	^a $230.538 \pm 5 \times 10^{-7}$	d (pc)	^b 9.9 ± 0.1
h ($\text{m}^2 \text{kg s}^{-1}$)	6.626×10^{-27}	A_{2-1} (s^{-1})	^c 6.911×10^{-7}
m_p (g)	1.673×10^{-24}	$B_0(\text{CO})$ (cm^{-1})	^d 1.923 ± 0.0023
m_{CO} (g)	$28 m_p$	c (cm s^{-1})	2.998×10^{10}
F_{2-1} (Jy km s^{-1})	^e 0.07	J_u	2
k ($\text{m}^2 \text{kg s}^{-2} \text{K}^{-1}$)	1.381×10^{-23}	T_{ex} (K)	^e 10 – 250

a: Winnewisser et al. (1997), b: van Leeuwen (2007), c: HITRAN (Gordon et al., 2017), d: Rank et al. (1965), e: This Work

Table 4.1: Input parameters and constants used to calculate an upper limit on total gas mass assuming LTE. Note that we use a range of excitation temperatures (T_{ex}) as the exact temperature is unknown. Superscript letters to the left of the value indicate the source of the value, listed at the bottom of the table.

Assuming local thermodynamic equilibrium (LTE), our 3σ upper flux limit corresponds to an upper limit on the total gas mass of $1.79 \times 10^{-7} M_{\oplus}$ to $9.06 \times 10^{-7} M_{\oplus}$ for a range of excitation temperatures from 10 K to 250 K, as seen in Figure 4.3(a). We assume this low range of excitation temperatures as it corresponds well with dust temperatures observed in debris disk outer belts and with low excitation temperatures for debris disks with multi-line measurements, and thus excitation temperature constraints. The latter of these, placed by Kóspál et al. (2013) and Matrà et al. (2017a), are found to be very low around ~ 10 K. Note that as the excitation temperature increases so too does the total mass, as there will be more states populated in the gas at higher J energy states, according to Boltzmann distributions, and therefore the gas mass must be correspondingly higher for the lower J levels to be sufficiently populated to reproduce the observed CO(2-1) flux density. A calculation using equations 10 – 12 found in Matrà et al. (2015) gives us a range of non local thermodynamic equilibrium (NLTE) gas mass upper limits (Figure 4.3(b)), over the same range of kinetic temperatures (T_k)

for our LTE calculations. Note, however, that $T_k \neq T_{ex}$ in NLTE, in that radiative and spontaneous excitation dominates in NLTE, while $T_k = T_{ex}$ in LTE where collisional excitation dominates. In Figure 4.3(b) electrons are assumed to be the primary collision partner, where the right side of the plot expresses a higher probability of collisional processes and is in LTE, which matches up with our results for a gas mass in LTE from Figure 4.3(a). The left side shows a small electron density where radiative and spontaneous transitions will dominate without the presence of collisional transitions. Overall, the NLTE limits range from $1.47 \times 10^{-7} M_{\oplus}$ to $5.82 \times 10^{-6} M_{\oplus}$.

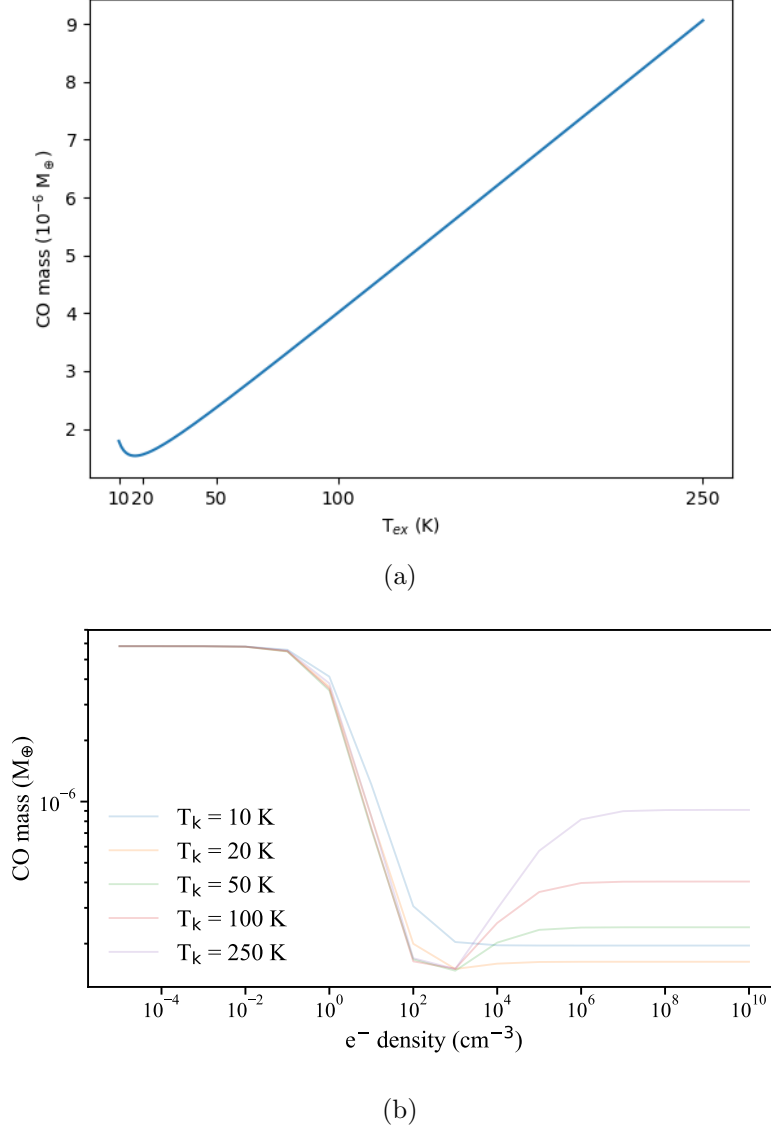


Figure 4.3: (a) Calculated LTE gas mass upper limits for a range of excitation temperatures based on possible theoretical temperatures found in debris disk systems and previous constraints on temperatures from gas detections in other systems. T_{ex} rises with CO mass due to Boltzmann statistics that define the number of molecules occupying higher energy states and higher temperatures (b) Calculated NLTE gas mass upper limits for a range of T_k and electron (e^{-}) densities. As NLTE is not described by the same collisional transitions as LTE it is necessary to use T_k values instead, as $T_{ex} \neq T_k$ in NLTE. The right side of the plot shows where the electron density is high enough to produce collisional transitions and describe the system in LTE, matching with our calculations from (a). Calculations for NLTE mass limits were performed by Luca Matr .

4.2.2 49 Ceti HCN(4-3)

To calculate an upper limit on the total HCN(4-3) mass in 49 Ceti we once again use Equation 4.1 and parameters listed in Table 4.2. As there are previous detections of CO in the disk we are able to use a single excitation temperature constrained by Hughes et al. (2017) at 32 K. Additionally, we assume that the system is in LTE for our calculation. Our calculation produces a singular upper limit (due to the singular T_{ex}) at $2.35 \times 10^{-7} M_{\oplus}$.

Parameter	Value	Parameter	Value
ν_0 (GHz)	^a 354.505	d (pc)	^b 61
h ($\text{m}^2 \text{kg s}^{-1}$)	6.626×10^{-27}	A_{4-3} (s^{-1})	^c 2.061×10^{-3}
m_p (g)	1.673×10^{-24}	$B_0(\text{HCN})$ (cm^{-1})	^d 1.471
m_{HCN} (g)	$27 m_p$	c (cm s^{-1})	2.998×10^{10}
F_{4-3} (Jy km s^{-1})	^e 0.09	J_u	4
k ($\text{m}^2 \text{kg s}^{-2} \text{K}^{-1}$)	1.381×10^{-23}	T_{ex} (K)	^f 32

a: DeLucia and Gordy (1969); van den Heuvel et al. (1982) b: van Leeuwen (2007), c: HITRAN Gordon et al. (2017), d: Winnewisser et al. (1971), e: This Work, f: Hughes et al. (2017)

Table 4.2: Input parameters and constants used to calculate an upper limit on total gas mass for 49 Ceti HCN(4-3) assuming LTE. Note that, unlike for AU Mic, we are able to use a single excitation temperature (T_{ex}) as constrained in previous observations. Superscript letters to the left of the value indicate the source of the value, listed at the bottom of the table.

4.3 Exocometary Ice Mass Fraction and Line Ratio

4.3.1 AU Mic CO(2-1)

Using equations 1 and 2 from Matr  et al. (2017b), shown as Equation 4.2 below, we are able to calculate an ice mass fraction for CO+CO₂ gas in exocomets for AU Mic. Assuming that gas in the disk is secondary in origin and that the system is in a

steady state, in that the outgassing rate of CO+CO₂ is equal to the destruction rate of CO due to photodissociation (\dot{M}_{CO}/t_{phd}), constraints on a CO+CO₂ ice mass fraction allow for a better understanding of the exact origin of the gas. Equation 4.2 is derived from $f_{CO+CO_2} = (1 + \dot{M}_D/\dot{M}_{CO+CO_2})^{-1}$, where $M_D = 6.7 \times 10^{-5} R^2 f L_* M_*^{-1}$. In the resulting Equation 4.2, R is the outer radius of the disk, ΔR is the difference between the outer disk radius and inner disk radius, $f = L_{IR}/L_*$ and is the fractional infrared luminosity of the disk, M_* is the mass of the star, t_{phd} is the photodissociation timescale of the molecule, and $M_{CO_{obs}}$ is the total gas mass of the molecule in the disk. Values for these parameters as well as their sources are given in Table 4.3 below. From Equation 4.2 we are able to calculate a CO+CO₂ ice mass fraction of exocomets at 0.0086–0.0097 for AU Mic based on our range of gas masses.

$$f_{CO+CO_2} = \frac{1}{1 + 0.0012(R^{1.5}\Delta R^{-1}f^2L_*M_*^{-0.5}t_{phd}M_{CO_{obs}}^{-1})} \quad (4.2)$$

Parameter	Value	Parameter	Value
R (au)	^a 40.3	M_* (M_\odot)	^c 0.31
ΔR (au)	^a 31.5	τ_{phd} (yrs)	^d 120
f	^b 3.9×10^{-4}	M_{CO} (M_\oplus)	^e $1.79 - 9.06 \times 10^{-7}$
L_* (L_\odot)	^c 0.09		

a: MacGregor et al. (2013) b: Matthews et al. (2015), c: Plavchan et al. (2009),
d: Kamp and Bertoldi (2000); Matr  et al. (2017b), e: This Work,

Table 4.3: Input parameters used to calculate an exocometary ice mass fraction for CO+CO₂ in AU Mic. We assume that the nature of the gas is secondary and expelled in the form of exocometary outgassing. Superscript letters to the left of the value indicate the source of the value, listed at the bottom of the table.

4.3.2 49 Ceti HCN(4-3)

For HCN(4-3) in 49 Ceti we determine a line flux ratio between the integrated flux of HCN(4-3)/CO(3-2). We use our upper limit for HCN(4-3) = $0.09 \text{ Jy km s}^{-1}$ and the flux detection of CO(3-2) = 6.0 Jy km s^{-1} taken from Hughes et al. (2017). We calculate an HCN(4-3)/CO(3-2) ratio of 0.015, which is a quantity of interest in determining the origin of the gas (Section 5.2.2).

As Matrà et al. (2018) points out in equations 1-3 of their work it is possible to calculate the fractional ice limit of HCN in exocomets if you make several key assumptions. The first being that as CO (and/or CO_2) is the dominant ice species outgassing in exocomets, it would not be valid to calculate the ice mass fraction of HCN (f_{HCN}) in the same manner as we did for AU Mic using Equation 4.2. Instead we would have to make the assumption that HCN is the dominant species in exocomets, which is widely believed to be untrue due to observations of comets within our own solar system. We would also have to assume protoplanetary abundances of HCN and CO in order to determine their respective outgassing rates to calculate f_{HCN} . Unfortunately, in the time allotted, we were unable to calculate f_{HCN} . We hope to be able to calculate it in the near future, as it will be important in either showing how well our measurements allow us to constrain the composition of the gas or in concluding that, due to the short photodissociation timescales of HCN, the gas will not be able to be observed even when in high abundances.

CHAPTER 5

DISCUSSION

...‘Where do we go from here?’ I heard one of sailor boys ask our Captain. Forward, ever forward into the piercing dark where we lose ourselves of place and time. And then forward again, to lose ourselves of being. The words were not a whisper, but loudly known to...

5.1 Comparison of Results

Before we contemplate the full implications of our results, let us first consider their relation to similar studies and results found in debris disks. Through comparison we can first determine whether our system seems to be routine or rather abnormal, and therefore what scenarios our specific results can describe.

5.1.1 AU Mic

With our range of gas mass upper limits on CO(2-1) we are able to compare them with detections and upper limits in other systems for evaluation. Although, as this work presents the deepest ever search for CO in an M star debris disk, it is difficult to directly compare with such a small to nonexistent sample size of debris disks around M

stars. Instead, we must compare our measurements to the slightly larger FGK stars and massively larger AB stars. To effectively compare the gas measurements we must first normalize our integrated flux upper limits to a distance of 100 pc. As our measurement is simply an integrated flux, our close neighbor AU Mic’s distance of 9.9 pc (van Leeuwen, 2007) would affect its integrated flux comparison to farther stars. The total integrated flux is scaled using Equation 5.1. Before scaling our upper limit total flux has a value of $0.07 \text{ Jy km s}^{-1}$. But scaled to a distance of 100 pc, we find our upper limit at a value of $6.86 \times 10^{-4} \text{ Jy km s}^{-1}$.

$$F_{normalized} = F_{integrated} * \left(\frac{d}{100 \text{ pc}}\right)^2 \quad (5.1)$$

Detections of gas around FGK stars typically have a scaled integrated flux value between 10^{-3} and $10^{-2} \text{ Jy km s}^{-1}$, while AB stars are even higher in the range between 10^{-1} and $10^1 \text{ Jy km s}^{-1}$, noting a slight negative relation to stellar age, in that older debris disks tend to be fainter (Hughes et al., 2018). Figure 5.1 shows a compilation of searches in debris disks for CO, noting upper limits and also detections for varying spectral types and CO transitions. The line fluxes are presented as a function of stellar age.

As one can quite clearly see, our AU Mic upper limits is at least 1 – 2 orders of magnitude fainter than the ‘typical’ gas-bearing debris disks around FGK stars, and 3 – 5 orders fainter than massive AB stars. AU Mic’s corresponding upper gas mass limit at $1.79\text{--}9.06 \times 10^{-7} M_{\oplus}$, however, does compare quite directly with the detection of CO in the A star Fomalhaut’s disk, found at $0.65\text{--}42 \times 10^{-7} M_{\oplus}$ (Matrà et al., 2017b). Additionally, the upper gas mass limits on AU Mic are similar to upper limits and detections placed on gas in smaller FGK star debris disks, such as HD 61005 ($6.9 \times 10^{-7} M_{\oplus}$) from Olofsson et al. (2016) and HD 181327 ($1.2\text{--}2.9 \times 10^{-6} M_{\oplus}$) from Marino et al. (2016). As addressed in Section 1.2, the sample size of M star debris disks observed for gas emission is quite nonexistent (Lestrade et al., 2006), preventing a direct comparison of our limits. Furthermore, as there is currently only one other spatially resolved disk

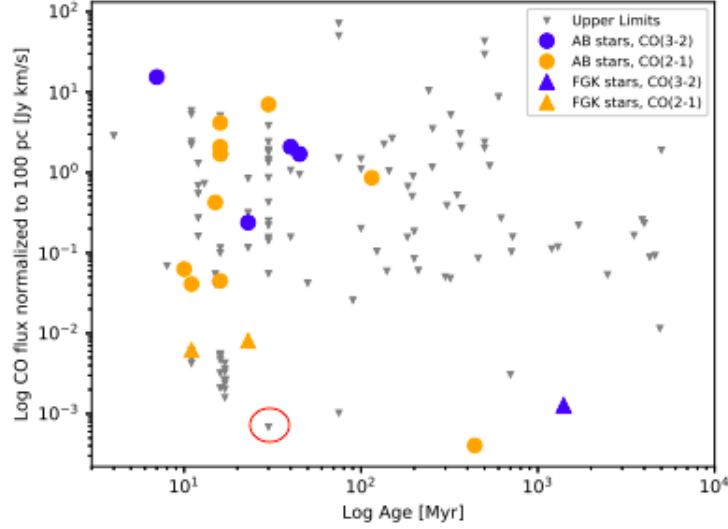


Figure 5.1: A compilation of debris disks with line flux detections or upper limits of CO(3-2 or 2-1) normalized to a distance of 100 pc as a function of spectral type and stellar age. The majority of detections occur at young stellar ages and more massive (AB) spectral types. FGK detections are also connected to younger stars, but appear to have much lower line fluxes. The upper limits seem to have no consistent grouping and are widespread across the plot. Our scaled upper limit on CO(2-1) in AU Mic is circled in red in the lower left hand corner. One can see just how low it really is compared to other upper limits and detections. The figure is taken from Hughes et al. (2018).

around an M star, that of GJ 581 (Lestrade et al., 2012), there may be little chance to grow the sample size and probe for gas in M star debris disks in the close future. Our limit is, however, consistent with model predictions for AU Mic conducted by Kral et al. (2017). They develop a CO gas mass model assuming the production of gas produced from debris in the collisional cascade and predict a gas mass of $M_{CO} = 4.8 \times 10^{-9} M_{\oplus}$, a value two orders of magnitude lower than our constrained limit. This means that the detection of CO gas in an M star debris disk will most likely require an instrument with sensitivity several orders of magnitude better than ALMA!

5.1.2 49 Ceti

To recap, in 49 Ceti we similarly place an upper limit on HCN(4-3) at $0.09 \text{ Jy km s}^{-1}$. As there are no current detections of any other molecule other than CO in debris disks we must likewise rely on a small sample of HCN limits in larger disks for direct comparison of our values. The only other upper limit of note for HCN comes from β Pic, with an upper limit value on HCN(3-2) at $\leq 2.0 \text{ Jy km s}^{-1}$ (Matrà et al., 2018). Similarly, they utilize the same spatial-spectral shift method in determination of their upper limit. We scale this upper limit from Matrà et al. (2018) and β Pic to the distance of 49 Ceti at 59 pc (van Leeuwen, 2007), resulting in a scaled upper limit of $0.21 \text{ Jy km s}^{-1}$. We note the extreme sensitivity difference in observations, as Matrà et al. (2018) observed β Pic with the less-sensitive Submillimeter Array (SMA). Of course, upper limits are not detections...but using ALMA these upper limits are extremely sensitive upper limits!

5.2 Primordial or Exocometary?

In analyzing the gas (or lack thereof) around a debris disk one of the important characteristics is whether or not the gas is primordial or secondary in nature. In other words, is the gas leftover from the protoplanetary disk or is it from a secondary source, such as a comet. There are a number of different ways this can be estimated, and here we shall provide two different methods and their corresponding impacts on the systems analyzed in this work.

5.2.1 49 Ceti: Background Evidence

Of the many studies focused on 49 Ceti, most agree that the gas component is of secondary nature due to volatile-rich planetesimals in the system. Higuchi et al. (2017) detect C[I] in the disk and place a C[I]/CO(3-2) integrated intensity ratio at 1.8 ± 0.4 and a C/CO column density of 54 ± 19 . These ratios are much larger than those detected in protoplanetary disks, with C[I]/CO = $0.05 - 0.9$ (Kama et al., 2016; Tsukagoshi et al.,

2015) and also those detected in molecular and diffuse clouds where $C/CO = 0.2 - 2.5$ (Ikeda et al., 1999; Ingalls et al., 1997). The high ratios indicate high amounts of C, which would be used up in chemical reactions to make CO if H_2 were present. But without this H_2 presence, it is implied that the large amounts of C are leftover from photodissociation of the CO molecule, which occurs on the timescale order of ~ 100 yr Higuchi et al. (2017).

Another indicator as to the origin of the gas is the spatial distribution of dust and gas in the disk. If gas is created through collisional interactions between dust and planetesimals then one would expect to find the gas and dust in similar locations within the disk. Varying locations would indicate different origins of the gas and the dust. However, Hughes et al. (2017) show that 49 Ceti fits neither description, with its dust and gas having both different radial dependencies and different inner/outer extents. These differences, although not necessarily fitting in to the canonical mold of secondary origins, still separate it far enough from a primordial explanation.

Finally, we must address the necessary production rates for secondary gas. In order for the disk to retain a detectable amount of CO gas and not lose it all due to photodissociation it is necessary for the system to continually create or replenish the CO in the disk. Kóspál et al. (2013) and Dent et al. (2014) suggest that large (Hale-Bopp scale) and frequent (minute timescales) cometary collisions are necessary to successfully replenish gas in debris disks. Kral et al. (2017), through the same modeling described in Section 5.1.1 show that it is more than likely to replenish the gas in 49 Ceti through collisions, as they calculate $0.1 < M_{obs}/M_{predicted} < 10$, a ratio indicating the possibility for secondary gas creation.

5.2.2 49 Ceti: HCN/CO

Adding another penny to the jar we discuss the impact that HCN/CO line flux ratios may have on revealing the origin of debris disk gas. As there are no detections of HCN in debris disks we must compare our ratio of HCN/CO to non-debris-disk systems and

objects. If we can match the ratio in 49 Ceti to a ratio in another disk type or solar system object then we can make certain (limited) assumptions about the origin of the gas.

We compare our upper integrated flux limit of $0.09 \text{ Jy km s}^{-1}$ for HCN(4-3) in 49 Ceti with the integrated flux limit of $6.0 \pm 0.1 \text{ Jy km s}^{-1}$ for CO(3-2) placed by Hughes et al. (2017). We calculate the HCN(4-3)/CO(3-2) flux ratio in 49 Ceti to be 0.015. Note that we only calculate a line flux ratio within this particular spectral band, and not a true abundance ratio. Le Roy et al. (2015) and Womack et al. (2017) comprised a collection of HCN/CO outgassing abundance ratios from 15 solar system comets, with values on the order of $10^0 - 10^{-3}$. While we only show a line ratio, our HCN/CO ratio is on the lower end this range calculated in solar system comets, which one would say excludes our gas from being the result of cometary outgassing. Some studies have shown, however, that our ratio would fit within the range from certain comets, who have an HCN/CO range between 0.012–0.041 (Biver et al., 2002), but outside of the norm at 0.01 – 0.4 (Biver and Bockelée-Morvan, 2016). This larger range by Biver et al. (2002) may be due to the variety of comets sampled at an extreme distance discrepancy, and also within several different cometary groups (Jupiter & Halley family, long period orbitals). It is also difficult to compare our ratio for 49 Ceti with those found in solar system comets due to the major difference in orbital distances. Solar system comets are often observed when their orbits are very close to the Sun, while most of the gas in 49 Ceti is hundreds of au away from the star. Temperature and excitation conditions vary greatly between those scales and it is plausible to consider that flux ratios for different molecules may vary greatly, as well. Additionally, A stars like 49 Ceti with higher UV/x-ray flux can photodissociate different molecules and may have a large effect on HCN/CO line ratios, as HCN photodissociates on a much shorter timescale than CO. Ignoring this side digression let us consider that our ratio for 49 Ceti HCN/CO is outside of the expected cometary range and thus not secondary (exocometary). We must then determine whether the gas is primordial or not through the comparison of

our HCN/CO ratio with those found in protoplanetary disks. While it is not known whether gas abundances change throughout the evolution of the disk, we shall assume that primordial gas in debris disks, as it is directly left over from the protoplanetary disk, retains a constant abundance. A survey by Öberg et al. (2010) shows 6 protoplanetary disks' HCN/CO ratio to be in the range of 0.06 – 0.33. Our 49 Ceti HCN/CO ratio of 0.015 is outside of this range constrained by Öberg et al. (2010), indicating that the gas is not of primordial nature either. From this cursory analysis it appears that we have eliminated all obvious explanations for the presence of HCN.

One remaining explanation for our HCN/CO ratio, similar to the issue of orbital distance addressed above, is an underlying change in composition of the molecules. Namely, in that HCN is chemically altered throughout its journey to present day debris disks. If we assume that the creation of secondary gas is from interactions between volatile-rich planetesimals then we conclude that gas in the system will be replenished as gas is released through the mass-loss process of collisions (Kral et al., 2017). The change in the mass of gas $\dot{M}_{gas} = \gamma \dot{M}_{loss}$ ¹ is taken from (Wyatt, 2008), where γ is a constant collisional transition rate defined by Matrà et al. (2015). However, Fray et al. (2005) show that HCN is photodissociated into CN, varying with the distance from the star. At larger distances (> 3 au) CN is created solely from the photodissociation of HCN. As the CO gas in 49 Ceti exists at large distances ($>> 3$ au), we could conclude that it is not likely to observe HCN, as it has a shorter timescale than CO and would likely photodissociate into its daughter molecule, CN. The photodissociation timescale is defined in equation 6 by Kral et al. (2017), where the dependence on cross section (σ_ν) and line frequencies (ν_i) may be adjusted as per the molecule using cross sections from Heays et al. (2017). A rapid photodissociation from HCN to CN, which is shown to have a higher production rate than HCN (Fray et al., 2005), would account for the lack of HCN and provide an explanation for the unique HCN/CO ratios. CN would

¹While Wyatt (2008) calculate \dot{M}_{gas} for CO, we make the assumption that outgassing rates are proportional to ice fractions and thus may be applied to other molecules (Matrà et al., 2017b)

therefore be a better candidate for molecular gas observations than HCN (Matrà et al., 2018), as planned observations of 49 Ceti will hopefully show.

CHAPTER 6

CONCLUSION

*...every tired man fears the sweet time to sit at the old
brickshaw table in the corner away from the strength of the
breeze, to see the ships shake with enthusiasm, and with
wrinkled hands to feel the etching of names left behind in
the wood.*

The study of the amount and frequency of molecular gas in debris disks provides a unique window into the active evolution of a star and its planet-forming disk. We present ALMA observations probing for CO(2-1) in AU Microscopii (M1) at 230.5380000 GHz and HCN(4-3) in 49 Ceti (A1V) at 354.5054759 GHz, nearby stars with debris disks. Analysis of the 3D image cube (channel maps) show no obvious gas presence. We reproduce a spectral-spatial shifting method developed by Matr  et al. (2017b) to determine the effect of varying assumptions regarding the disk velocity field on the SNR of the resulting spectrum. Systems with known molecular emission detections allow for the implementation of any of three velocity fields based on the velocities of the detected emission, the Moment 1 map, or a standard Keplerian rotation stellar debris disk model field. We demonstrate that velocity fields based on previous molecular detections as well as the Moment 1 maps provide the highest SNR, as they are directly based off of gas observations and detections. At the current time, it appears that a standard

Keplerian rotation velocity field results in a lower SNR than the other two field models. Analysis of the three fields (Section 3.2.1) using previous detections of CO(3-2) in 49 Ceti (Hughes et al., 2008, 2017) shows that velocity fields based on previous gas detections has an increase to the SNR on the order of 2 – 3 factors over a standard Keplerian field. Applying the known velocity field from CO(3-2) observations of 49 Ceti therefore allows us to place extremely stringent limits on the HCN(4-3) emission from the disk. When searching for never-before-observed emission lines in debris disks this higher SNR could be the difference between the ability to detect faint signals or not (or at least place more sensitive upper limits).

Our observations present the most sensitive search to date for CO emission from an M star debris disk, and one of the only deep searches for molecules other than CO in a debris disk, in our case, HCN in 49 Ceti. Using a spectral-spatial shifting method we place 3σ upper limits at $0.07 \text{ Jy km s}^{-1}$ and $0.09 \text{ Jy km s}^{-1}$ for CO(2-1) in AU Mic and HCN(4-3) in 49 Ceti, respectively. Upper limits for the total gas mass in each system are calculated using Equation 4.1 taking into account excitation temperatures in LTE, producing values on the order of $10^{-7} M_{\oplus}$. A range of 10 – 250 K excitation temperatures was used for AU Mic, while a constrained excitation temperature of 32 K (Hughes et al., 2017) was used for 49 Ceti. Additionally, NLTE calculations for AU Mic results in a similar upper limit as those done assuming LTE, on the order of $10^{-7} - 10^{-6} M_{\oplus}$. Fractional exocometary ice limits are placed between 0.0086 – 0.0097 for AU Mic CO+CO₂. For 49 Ceti we calculate an HCN(4-3)/CO(3-2) ratio of 0.015.

The results for both systems present interesting case studies for the evolution of debris disks and the gas within them. AU Mic’s CO levels aren’t just low...they are shockingly low (up to 3 orders of magnitude lower) (Hughes et al., 2018; Matthews et al., 2014; Wyatt, 2008) than is commonly observed even in a debris disk, taking into account factors such as spectral type and disk scale. Our consideration of ‘gas-expectations’ in a debris disk is based on current known detections and models to simulate gas mass amounts (Kral et al., 2017) and upper limits of varying debris disks

of multiple spectral types. Comparison for the upper gas mass limit on AU Mic CO(2-1) is difficult due to the lack of sample size regarding M star debris disk gas observations. Kral et al. (2017), through the use of their model, predict AU Mic’s gas mass for CO to be $4.8 \times 10^{-9} M_{\oplus}$, which is consistent with our upper limit. Outside of models, we are forced to compare our limits to much larger stars and hotter spectral types, which is likely not a worthy comparison due to the varying scales of their debris disks, as well as the different temperatures, masses, and photodissociating radiation from the central star. One of the few with a gas mass similar to the upper limit set on AU Mic is the A star Fomalhaut, which was previously indicated to have an upper limit of CO gas on the order of $10^{-4} M_{\oplus}$ (Matrà et al., 2015) now shows a detection of CO gas on the order of $10^{-7} M_{\oplus}$ (Matrà et al., 2017b). For AU Mic it is unlikely that an actual gas mass detection (if found) would correspond directly to its current upper limit of $10^{-7} M_{\oplus}$. Thus given recent results for Fomalhaut’s system we must conclude that the true gas mass in AU Mic is even lower than our upper limit indicates, which would be a shockingly low amount of gas!

In 49 Ceti, however, our upper limit for HCN(4-3) appears to be stuck in no-man’s land. The HCN/CO line and cometary outgassing abundance ratios have been previously determined for varying systems and objects, such as protoplanetary disks (Öberg et al., 2010) and comets (Biver et al., 2002). Since the ratio is observed to be very different for disks (0.06 – 0.33) than for comets (0.01 – 0.4), comparing the ratio observed for 49 Ceti with these values may provide an initial indication of whether its composition is more similar to a disk or an exocomet.

We also note the cautious element of using solar system cometary outgassing ratios, as discussed in Section 5.2.2, that the occurrence of secondary gas production through exocomets takes place at upwards of several hundreds of au from the star, while our current observations of gas composition in comets is limited to objects within much smaller Solar System scales. Additionally, the difference in spectral type may play a factor in the photodissociation of HCN, as A stars like 49 Ceti have much higher UV/x-

ray radiation than solar spectral types. However, our HCN/CO upper limit ratio of < 0.015 indicates that there is too little HCN for it to be of exocometary origin or for it to be a remnant from the early life of the disk in the protoplanetary stage. With such inconclusive results it is difficult to make statements about gas in debris disks as a whole. Quite simply put, these are new results that do not match up with what we have seen in the past. This raises the possibility for a new explanation, such as those proposed by Matr  et al. (2018) and Kral et al. (2016), which suggest a change to the chemical composition over the lifetime of a disk. Even though the anomalous HCN/CO ratio is surprising, it may still be telling us something about excitation conditions and/or the prevalence of photodissociation in debris disks, particularly those bearing gas. While the need for further observations and modeling is always obvious, 49 Ceti has given us a wonderful clue and stepping stone into the more intricate designs of debris disks. After all, “No detections are detections, too.”

BIBLIOGRAPHY

- H. H. Aumann. IRAS observations of matter around nearby stars. , 97:885–891, October 1985. doi: 10.1086/131620.
- E. A. Bergin and J. P. Williams. The Determination of Protoplanetary Disk Masses. In M. Pessah and O. Gressel, editors, *Astrophysics and Space Science Library*, volume 445 of *Astrophysics and Space Science Library*, page 1, 2017. doi: 10.1007/978-3-319-60609-5_1.
- H. Beust, A. M. Lagrange-Henri, A. V. Madjar, and R. Ferlet. The Beta Pictoris circumstellar disk. X - Numerical simulations of infalling evaporating bodies. , 236: 202–216, September 1990.
- N. Biver and D. Bockelée-Morvan. Chemical diversity in the comet population. *IAU Focus Meeting*, 29(27):228–232, October 2016. doi: 10.1017/S1743921316002945.
- N. Biver, D. Bockelée-Morvan, J. Crovisier, P. Colom, F. Henry, R. Moreno, G. Paubert, D. Despois, and D. C. Lis. Chemical Composition Diversity Among 24 Comets Observed At Radio Wavelengths. *Earth Moon and Planets*, 90:323–333, March 2002.
- A. Boccaletti, E. Sezestre, A.-M. Lagrange, P. Thébault, R. Gratton, M. Langlois, C. Thalmann, M. Janson, P. Delorme, J.-C. Augereau, G. Schneider, J. Milli, C. Grady, J. Debes, Q. Kral, J. Olofsson, J. Carson, A. L. Maire, T. Henning, J. Wisniewski, J. Schlieder, C. Dominik, S. Desidera, C. Ginski, D. Hines, F. Ménard,

- D. Mouillet, N. Pawellek, A. Vigan, E. Lagadec, H. Avenhaus, J.-L. Beuzit, B. Biller, M. Bonavita, M. Bonnefoy, W. Brandner, F. Cantalloube, G. Chauvin, A. Cheetham, M. Cudel, C. Gry, S. Daemgen, M. Feldt, R. Galicher, J. Girard, P. Janin-Potiron, M. Kasper, H. Le Coroller, D. Mesa, S. Peretti, C. Perrot, M. Samland, E. Sissa, F. Wildi, S. Rochat, E. Stadler, L. Gluck, A. Origné, M. Llored, P. Baudoz, G. Rousset, P. Martinez, and F. Rigal. Observations of fast-moving features in the debris disk of AU Mic on a three-year timescale: Confirmation and new discoveries. *ArXiv e-prints*, March 2018.
- A. Carmona, M. E. van den Ancker, T. Henning, M. Goto, D. Fedele, and B. Stecklum. A search for near-infrared molecular hydrogen emission in the CTTS LkH α 264 and the debris disk 49 Ceti. , 476:853–862, December 2007. doi: 10.1051/0004-6361:20078536.
- A. Carmona, M. E. van den Ancker, T. Henning, Y. Pavlyuchenkov, C. P. Dullemond, M. Goto, D. Fedele, B. Stecklum, W.-F. Thi, J. Bouwman, and L. B. F. M. Waters. Searching for H₂ emission from protoplanetary disks using near- and mid-infrared high-resolution spectroscopy. In Y.-S. Sun, S. Ferraz-Mello, and J.-L. Zhou, editors, *Exoplanets: Detection, Formation and Dynamics*, volume 249 of *IAU Symposium*, pages 359–368, May 2008. doi: 10.1017/S1743921308016827.
- J. M. Carpenter, E. E. Mamajek, L. A. Hillenbrand, and M. R. Meyer. Debris Disks in the Upper Scorpius OB Association. , 705:1646–1671, November 2009. doi: 10.1088/0004-637X/705/2/1646.
- E. Chiang and J. Fung. Stellar Winds and Dust Avalanches in the AU Mic Debris Disk. , 848:4, October 2017. doi: 10.3847/1538-4357/aa89e6.
- É. Choquet, J. Milli, Z. Wahhaj, R. Soummer, A. Roberge, J.-C. Augereau, M. Booth, O. Absil, A. Boccaletti, C. H. Chen, J. H. Debes, C. del Burgo, W. R. F. Dent, S. Ertel, J. H. Girard, E. Gofas-Salas, D. A. Golimowski, C. A. Gómez González, J. Brendan Hagan, P. Hibon, D. C. Hines, G. M. Kennedy, A.-M. Lagrange, L. Matrà, D. Mawet,

- D. Mouillet, M. N'Diaye, M. D. Perrin, C. Pinte, L. Pueyo, A. Rajan, G. Schneider, S. Wolff, and M. Wyatt. First Scattered-light Images of the Gas-rich Debris Disk around 49 Ceti. , 834:L12, January 2017. doi: 10.3847/2041-8213/834/2/L12.
- A. Czechowski and I. Mann. Collisional Vaporization of Dust and Production of Gas in the β Pictoris Dust Disk. , 660:1541–1555, May 2007. doi: 10.1086/512965.
- P. D'Alessio, N. Calvet, and D. S. Woolum. Thermal Structure of Protoplanetary Disks. In A. N. Krot, E. R. D. Scott, and B. Reipurth, editors, *Chondrites and the Protoplanetary Disk*, volume 341 of *Astronomical Society of the Pacific Conference Series*, page 353, December 2005.
- Frank DeLucia and Walter Gordy. Molecular-beam maser for the shorter-millimeter-wave region: Spectral constants of hcn and dcn. *Phys. Rev.*, 187:58–65, Nov 1969. doi: 10.1103/PhysRev.187.58. URL <https://link.aps.org/doi/10.1103/PhysRev.187.58>.
- W. R. F. Dent, J. S. Greaves, and I. M. Coulson. CO emission from discs around isolated HAeBe and Vega-excess stars. , 359:663–676, May 2005. doi: 10.1111/j.1365-2966.2005.08938.x.
- W. R. F. Dent, M. C. Wyatt, A. Roberge, J.-C. Augereau, S. Casassus, S. Corder, J. S. Greaves, I. de Gregorio-Monsalvo, A. Hales, A. P. Jackson, A. M. Hughes, A.-M. Lagrange, B. Matthews, and D. Wilner. Molecular Gas Clumps from the Destruction of Icy Bodies in the β Pictoris Debris Disk. *Science*, 343:1490–1492, March 2014. doi: 10.1126/science.1248726.
- J. S. Dohnanyi. Collisional Model of Asteroids and Their Debris. , 74:2531–2554, May 1969. doi: 10.1029/JB074i010p02531.
- M. Duflot, P. Figon, and N. Meyssonnier. Vitesses radiales. Catalogue WEB: Wilson Evans Batten. Subtitle: Radial velocities: The Wilson-Evans-Batten catalogue. *Astronomy and Astrophysics Supplement Series*, 114:269, December 1995.

- C. P. Dullemond, C. Dominik, and A. Natta. Passive Irradiated Circumstellar Disks with an Inner Hole. , 560:957–969, October 2001. doi: 10.1086/323057.
- C. P. Dullemond, D. Hollenbach, I. Kamp, and P. D’Alessio. Models of the Structure and Evolution of Protoplanetary Disks. *Protostars and Planets V*, pages 555–572, 2007.
- A. Dutrey, D. Semenov, E. Chapillon, U. Gorti, S. Guilloteau, F. Hersant, M. Hogerheijde, M. Hughes, G. Meeus, H. Nomura, V. Piétu, C. Qi, and V. Wakelam. Physical and Chemical Structure of Planet-Forming Disks Probed by Millimeter Observations and Modeling. *Protostars and Planets VI*, pages 317–338, 2014. doi: 10.2458/azu_uapress_9780816531240-ch014.
- C. C. Espaillat, Á. Ribas, M. K. McClure, J. Hernández, J. E. Owen, N. Avish, N. Calvet, and R. Franco-Hernández. An Incipient Debris Disk in the Chamaeleon I Cloud. , 844:60, July 2017. doi: 10.3847/1538-4357/aa7a10.
- M. P. Fitzgerald, P. G. Kalas, G. Duchêne, C. Pinte, and J. R. Graham. The AU Microscopii Debris Disk: Multiwavelength Imaging and Modeling. , 670:536–556, November 2007. doi: 10.1086/521344.
- K. France, A. Roberge, R. E. Lupu, S. Redfield, and P. D. Feldman. A Low-Mass H_2 Component to the AU Microscopii Circumstellar Disk. , 668:1174–1181, October 2007. doi: 10.1086/521348.
- N. Fray, Y. Bnilan, H. Cottin, M.-C. Gazeau, and J. Crovisier. The origin of the cn radical in comets: A review from observations and models. *Planetary and Space Science*, 53(12):1243 – 1262, 2005. ISSN 0032-0633. doi: <https://doi.org/10.1016/j.pss.2005.06.005>. URL <http://www.sciencedirect.com/science/article/pii/S0032063305001406>.
- E. Gaidos. A minimum mass nebula for M dwarfs. , 470:L1–L5, September 2017. doi: 10.1093/mnrasl/slx063.

- I.E. Gordon, L.S. Rothman, C. Hill, R.V. Kochanov, Y. Tan, P.F. Bernath, M. Birk, V. Boudon, A. Campargue, K.V. Chance, B.J. Drouin, J.-M. Flaud, R.R. Gamache, J.T. Hodges, D. Jacquemart, V.I. Perevalov, A. Perrin, K.P. Shine, M.-A.H. Smith, J. Tennyson, G.C. Toon, H. Tran, V.G. Tyuterev, A. Barbe, A.G. Császr, V.M. Devi, T. Furtenbacher, J.J. Harrison, J.-M. Hartmann, A. Jolly, T.J. Johnson, T. Karman, I. Kleiner, A.A. Kyuberis, J. Loos, O.M. Lyulin, S.T. Massie, S.N. Mikhailenko, N. Moazzen-Ahmadi, H.S.P. Mller, O.V. Naumenko, A.V. Nikitin, O.L. Polyansky, M. Rey, M. Rotger, S.W. Sharpe, K. Sung, E. Starikova, S.A. Tashkun, J. Vander Auwera, G. Wagner, J. Wilzewski, P. Wcislo, S. Yu, and E.J. Zak. The hitran2016 molecular spectroscopic database. *Journal of Quantitative Spectroscopy and Radiative Transfer*, 203:3 – 69, 2017. ISSN 0022-4073. doi: <https://doi.org/10.1016/j.jqsrt.2017.06.038>. URL <http://www.sciencedirect.com/science/article/pii/S0022407317301073>. HITRAN2016 Special Issue.
- J. R. Graham, P. G. Kalas, and B. C. Matthews. The Signature of Primordial Grain Growth in the Polarized Light of the AU Microscopii Debris Disk. , 654:595–605, January 2007. doi: 10.1086/509318.
- A. Grigorieva, P. Thébault, P. Artymowicz, and A. Brandeker. Survival of icy grains in debris discs. The role of photospattering. , 475:755–764, November 2007. doi: 10.1051/0004-6361:20077686.
- A. N. Heays, A. D. Bosman, and E. F. van Dishoeck. Photodissociation and photoionisation of atoms and molecules of astrophysical interest. , 602, June 2017. doi: 10.1051/0004-6361/201628742.
- A. E. Higuchi, A. Sato, T. Tsukagoshi, N. Sakai, K. Iwasaki, M. Momose, H. Kobayashi, D. Ishihara, S. Watanabe, H. Kaneda, and S. Yamamoto. Detection of Submillimeter-wave [C I] Emission in Gaseous Debris Disks of 49 Ceti and β Pictoris. , 839:L14, April 2017. doi: 10.3847/2041-8213/aa67f4.

- L. A. Hillenbrand, J. M. Carpenter, J. S. Kim, M. R. Meyer, D. E. Backman, A. Moro-Martín, D. J. Hollenbach, D. C. Hines, I. Pascucci, and J. Bouwman. The Complete Census of 70 μ m-Bright Debris Disks within “The Formation and Evolution of Planetary Systems” Spitzer Legacy Survey of Sun-like Stars. , 677:630–656, April 2008. doi: 10.1086/529027.
- D. Hollenbach, D. Johnstone, S. Lizano, and F. Shu. Photoevaporation of disks around massive stars and application to ultracompact H II regions. , 428:654–669, June 1994. doi: 10.1086/174276.
- A. M. Hughes, D. J. Wilner, I. Kamp, and M. R. Hogerheijde. A Resolved Molecular Gas Disk around the Nearby A Star 49 Ceti. , 681:626–635, July 2008. doi: 10.1086/588520.
- A. M. Hughes, J. Lieman-Sifry, K. M. Flaherty, C. M. Daley, A. Roberge, Á. Kóspál, A. Moór, I. Kamp, D. J. Wilner, S. M. Andrews, J. H. Kastner, and P. Ábrahám. Radial Surface Density Profiles of Gas and Dust in the Debris Disk around 49 Ceti. , 839:86, April 2017. doi: 10.3847/1538-4357/aa6b04.
- A. M. Hughes, G. Duchene, and B. Matthews. Debris Disks: Structure, Composition, and Variability. *ArXiv e-prints*, February 2018.
- M. Ikeda, H. Maezawa, T. Ito, G. Saito, Y. Sekimoto, S. Yamamoto, K. Tatematsu, Y. Arikawa, Y. Aso, T. Noguchi, S.-C. Shi, K. Miyazawa, S. Saito, H. Ozeki, H. Fujiwara, M. Ohishi, and J. Inatani. Large-Scale Mapping Observations of the C I (3P_1 - 3P_0) and CO ($J = 3-2$) Lines toward the Orion A Molecular Cloud. , 527:L59–L62, December 1999. doi: 10.1086/312395.
- S. Inaba, G. W. Wetherill, and M. Ikoma. Formation of gas giant planets: core accretion models with fragmentation and planetary envelope. , 166:46–62, November 2003. doi: 10.1016/j.icarus.2003.08.001.

- J. G. Ingalls, R. A. Chamberlin, T. M. Bania, J. M. Jackson, A. P. Lane, and A. A. Stark. Atomic Carbon in Southern Hemisphere High-Latitude Clouds. , 479:296–302, April 1997. doi: 10.1086/303876.
- A. Isella, L. M. Pérez, and J. M. Carpenter. On the Nature of the Transition Disk around LkCa 15. , 747:136, March 2012. doi: 10.1088/0004-637X/747/2/136.
- A. P. Jackson, M. C. Wyatt, A. Bonsor, and D. Veras. Debris froms giant impacts between planetary embryos at large orbital radii. , 440:3757–3777, June 2014. doi: 10.1093/mnras/stu476.
- T. L. Wilson K. Rohlfs. *Tools of Radio Astronomy*. Springer-Verlag, Germany, 3 edition, 2000. ISBN 354066016x.
- P. Kalas, M. C. Liu, and B. C. Matthews. Discovery of a Large Dust Disk Around the Nearby Star AU Microscopii. *Science*, 303:1990–1992, March 2004. doi: 10.1126/science.1093420.
- M. Kama, S. Bruderer, M. Carney, M. Hogerheijde, E. F. van Dishoeck, D. Fedele, A. Baryshev, W. Boland, R. Güsten, A. Aikutalp, Y. Choi, A. Endo, W. Frieswijk, A. Karska, P. Klaassen, E. Koumpia, L. Kristensen, S. Leurini, Z. Nagy, J.-P. Perez Beaupuits, C. Risacher, N. van der Marel, T. A. van Kempen, R. J. van Weeren, F. Wyrowski, and U. A. Yıldız. Observations and modelling of CO and [C I] in protoplanetary disks. First detections of [C I] and constraints on the carbon abundance. , 588:A108, April 2016. doi: 10.1051/0004-6361/201526791.
- I. Kamp and F. Bertoldi. CO in the circumstellar disks of Vega and beta Pictoris. , 353:276–286, January 2000.
- G. R. Knapp and F. J. Kerr. The galactic gas-to-dust ratio from observations of eighty-one globular clusters. , 35:361–379, October 1974.

- Á. Kóspál, A. Moór, A. Juhász, P. Ábrahám, D. Apai, T. Csengeri, C. A. Grady, T. Henning, A. M. Hughes, C. Kiss, I. Pascucci, and M. Schmalzl. ALMA Observations of the Molecular Gas in the Debris Disk of the 30 Myr Old Star HD 21997. , 776:77, October 2013. doi: 10.1088/0004-637X/776/2/77.
- Q. Kral, M. Wyatt, R. F. Carswell, J. E. Pringle, L. Matrà, and A. Juhász. A self-consistent model for the evolution of the gas produced in the debris disc of β Pictoris. , 461:845–858, September 2016. doi: 10.1093/mnras/stw1361.
- Q. Kral, L. Matrà, M. C. Wyatt, and G. M. Kennedy. Predictions for the secondary CO, C and O gas content of debris discs from the destruction of volatile-rich planetesimals. , 469:521–550, July 2017. doi: 10.1093/mnras/stx730.
- J. E. Krist, D. R. Ardila, D. A. Golimowski, M. Clampin, H. C. Ford, G. D. Illingworth, G. F. Hartig, F. Bartko, N. Benítez, J. P. Blakeslee, R. J. Bouwens, L. D. Bradley, T. J. Broadhurst, R. A. Brown, C. J. Burrows, E. S. Cheng, N. J. G. Cross, R. Demarco, P. D. Feldman, M. Franx, T. Goto, C. Gronwall, B. Holden, N. Homeier, L. Infante, R. A. Kimble, M. P. Lesser, A. R. Martel, S. Mei, F. Menanteau, G. R. Meurer, G. K. Miley, V. Motta, M. Postman, P. Rosati, M. Sirianni, W. B. Sparks, H. D. Tran, Z. I. Tsvetanov, R. L. White, and W. Zheng. Hubble Space Telescope Advanced Camera for Surveys Coronagraphic Imaging of the AU Microscopii Debris Disk. , 129:1008–1017, February 2005. doi: 10.1086/426755.
- L. Le Roy, K. Altwegg, H. Balsiger, J.-J. Berthelier, A. Bieler, C. Briois, U. Calmonte, M. R. Combi, J. De Keyser, F. Dhooghe, B. Fiethe, S. A. Fuselier, S. Gasc, T. I. Gombosi, M. Hässig, A. Jäckel, M. Rubin, and C.-Y. Tzou. Inventory of the volatiles on comet 67P/Churyumov-Gerasimenko from Rosetta/ROSINA. , 583:A1, November 2015. doi: 10.1051/0004-6361/201526450.
- J.-F. Lestrade, M. C. Wyatt, F. Bertoldi, W. R. F. Dent, and K. M. Menten. Search for cold debris disks around M-dwarfs. , 460:733–741, December 2006. doi: 10.1051/0004-6361:20065873.

- J.-F. Lestrade, B. C. Matthews, B. Sibthorpe, G. M. Kennedy, M. C. Wyatt, G. Bryden, J. S. Greaves, E. Thilliez, A. Moro-Martín, M. Booth, W. R. F. Dent, G. Duchêne, P. M. Harvey, J. Horner, P. Kalas, J. J. Kavelaars, N. M. Phillips, D. R. Rodriguez, K. Y. L. Su, and D. J. Wilner. A DEBRIS disk around the planet hosting M-star GJ 581 spatially resolved with Herschel. , 548:A86, December 2012. doi: 10.1051/0004-6361/201220325.
- J. Lieman-Sifry, A. M. Hughes, J. M. Carpenter, U. Gorti, A. Hales, and K. M. Flaherty. Debris Disks in the Scorpius-Centaurus OB Association Resolved by ALMA. , 828:25, September 2016. doi: 10.3847/0004-637X/828/1/25.
- M. C. Liu. Substructure in the Circumstellar Disk Around the Young Star AU Microscopii. *Science*, 305:1442–1444, September 2004. doi: 10.1126/science.1102929.
- M. A. MacGregor, D. J. Wilner, K. A. Rosenfeld, S. M. Andrews, B. Matthews, A. M. Hughes, M. Booth, E. Chiang, J. R. Graham, P. Kalas, G. Kennedy, and B. Sibthorpe. Millimeter Emission Structure in the First ALMA Image of the AU Mic Debris Disk. , 762:L21, January 2013. doi: 10.1088/2041-8205/762/2/L21.
- E. E. Mamajek. Initial Conditions of Planet Formation: Lifetimes of Primordial Disks. In T. Usuda, M. Tamura, and M. Ishii, editors, *American Institute of Physics Conference Series*, volume 1158 of *American Institute of Physics Conference Series*, pages 3–10, August 2009. doi: 10.1063/1.3215910.
- S. Marino, L. Matrà, C. Stark, M. C. Wyatt, S. Casassus, G. Kennedy, D. Rodriguez, B. Zuckerman, S. Perez, W. R. F. Dent, M. Kuchner, A. M. Hughes, G. Schneider, A. Steele, A. Roberge, J. Donaldson, and E. Nesvold. Exocometary gas in the HD 181327 debris ring. , 460:2933–2944, August 2016. doi: 10.1093/mnras/stw1216.
- S. Marino, M. C. Wyatt, O. Panić, L. Matrà, G. M. Kennedy, A. Bonsor, Q. Kral, W. R. F. Dent, G. Duchene, D. Wilner, C. M. Lisse, J.-F. Lestrade, and B. Matthews.

- ALMA observations of the η Corvi debris disc: inward scattering of CO-rich exocomets by a chain of 3-30 M_{γ} planets? , 465:2595–2615, March 2017. doi: 10.1093/mnras/stw2867.
- L. Matrà, O. Panić, M. C. Wyatt, and W. R. F. Dent. CO mass upper limits in the Fomalhaut ring - the importance of NLTE excitation in debris discs and future prospects with ALMA. , 447:3936–3947, March 2015. doi: 10.1093/mnras/stu2619.
- L. Matrà, W. R. F. Dent, M. C. Wyatt, Q. Kral, D. J. Wilner, O. Panić, A. M. Hughes, I. de Gregorio-Monsalvo, A. Hales, J.-C. Augereau, J. Greaves, and A. Roberge. Exocometary gas structure, origin and physical properties around β Pictoris through ALMA CO multitransition observations. , 464:1415–1433, January 2017a. doi: 10.1093/mnras/stw2415.
- L. Matrà, M. A. MacGregor, P. Kalas, M. C. Wyatt, G. M. Kennedy, D. J. Wilner, G. Duchene, A. M. Hughes, M. Pan, A. Shannon, M. Clampin, M. P. Fitzgerald, J. R. Graham, W. S. Holland, O. Panić, and K. Y. L. Su. Detection of Exocometary CO within the 440 Myr Old Fomalhaut Belt: A Similar CO+CO₂ Ice Abundance in Exocomets and Solar System Comets. , 842:9, June 2017b. doi: 10.3847/1538-4357/aa71b4.
- L. Matrà, D. J. Wilner, K. I. Öberg, S. M. Andrews, R. A. Loomis, M. C. Wyatt, and W. R. F. Dent. Molecular Reconnaissance of the β Pictoris Gas Disk with the SMA: A Low HCN/(CO+CO₂) Outgassing Ratio and Predictions for Future Surveys. , 853:147, February 2018. doi: 10.3847/1538-4357/aaa42a.
- B. C. Matthews, A. V. Krivov, M. C. Wyatt, G. Bryden, and C. Eiroa. Observations, Modeling, and Theory of Debris Disks. *Protostars and Planets VI*, pages 521–544, 2014. doi: 10.2458/azu_uapress.9780816531240-ch023.
- B. C. Matthews, G. Kennedy, B. Sibthorpe, W. Holland, M. Booth, P. Kalas, M. MacGregor, D. Wilner, B. Vandenbussche, G. Olofsson, J. Blommaert, A. Brandeker,

- W. R. F. Dent, B. L. de Vries, J. Di Francesco, M. Fridlund, J. R. Graham, J. Greaves, A. M. Heras, M. Hogerheijde, R. J. Ivison, E. Pantin, and G. L. Pilbratt. The AU Mic Debris Disk: Far-infrared and Submillimeter Resolved Imaging. , 811:100, October 2015. doi: 10.1088/0004-637X/811/2/100.
- G. Meeus, B. Montesinos, I. Mendigutía, I. Kamp, W. F. Thi, C. Eiroa, C. A. Grady, G. Mathews, G. Sandell, C. Martin-Zaïdi, S. Brittain, W. R. F. Dent, C. Howard, F. Ménard, C. Pinte, A. Roberge, B. Vandenbussche, and J. P. Williams. Observations of Herbig Ae/Be stars with Herschel/PACS. The atomic and molecular contents of their protoplanetary discs. , 544:A78, August 2012. doi: 10.1051/0004-6361/201219225.
- S. A. Metchev, J. A. Eisner, L. A. Hillenbrand, and S. Wolf. Adaptive Optics Imaging of the AU Microscopii Circumstellar Disk: Evidence for Dynamical Evolution. , 622: 451–462, March 2005. doi: 10.1086/427869.
- B. E. Miles, A. Roberge, and B. Welsh. UV Spectroscopy of Star-grazing Comets Within the 49 Ceti Debris Disk. , 824:126, June 2016. doi: 10.3847/0004-637X/824/2/126.
- B. Montesinos, C. Eiroa, A. V. Krivov, J. P. Marshall, G. L. Pilbratt, R. Liseau, A. Mora, J. Maldonado, S. Wolf, S. Ertel, A. Bayo, J.-C. Augereau, A. M. Heras, M. Fridlund, W. C. Danchi, E. Solano, F. Kirchschlager, C. del Burgo, and D. Montes. Incidence of debris discs around FGK stars in the solar neighbourhood. , 593:A51, September 2016. doi: 10.1051/0004-6361/201628329.
- A. Moór, P. Ábrahám, A. Juhász, C. Kiss, I. Pascucci, Á. Kóspál, D. Apai, T. Henning, T. Csengeri, and C. Grady. Molecular Gas in Young Debris Disks. , 740:L7, October 2011. doi: 10.1088/2041-8205/740/1/L7.
- A. Moór, T. Henning, A. Juhász, P. Ábrahám, Z. Balog, Á. Kóspál, I. Pascucci, G. M. Szabó, R. Vavrek, M. Curé, T. Csengeri, C. Grady, R. Güsten, and C. Kiss. Discovery

- of Molecular Gas around HD 131835 in an APEX Molecular Line Survey of Bright Debris Disks. , 814:42, November 2015. doi: 10.1088/0004-637X/814/1/42.
- A. Moór, M. Curé, Á. Kóspál, P. Ábrahám, T. Csengeri, C. Eiroa, D. Gunawan, T. Henning, A. M. Hughes, A. Juhász, N. Pawellek, and M. Wyatt. Molecular Gas in Debris Disks around Young A-type Stars. , 849:123, November 2017. doi: 10.3847/1538-4357/aa8e4e.
- É. Morey and J.-F. Lestrade. On the steady state collisional evolution of debris disks around M dwarfs. , 565:A58, May 2014. doi: 10.1051/0004-6361/201322567.
- D. Nesvorný, A. N. Youdin, and D. C. Richardson. Formation of Kuiper Belt Binaries by Gravitational Collapse. , 140:785–793, September 2010. doi: 10.1088/0004-6256/140/3/785.
- D. Nesvorný, D. Janches, D. Vokrouhlický, P. Pokorný, W. F. Bottke, and P. Jenniskens. Dynamical Model for the Zodiacal Cloud and Sporadic Meteors. , 743:129, December 2011. doi: 10.1088/0004-637X/743/2/129.
- K. I. Öberg, C. Qi, J. K. J. Fogel, E. A. Bergin, S. M. Andrews, C. Espaillat, T. A. van Kempen, D. J. Wilner, and I. Pascucci. The Disk Imaging Survey of Chemistry with SMA. I. Taurus Protoplanetary Disk Data. , 720:480–493, September 2010. doi: 10.1088/0004-637X/720/1/480.
- R. Ohsawa, T. Onaka, and C. Yasui. Impact of the initial disk mass function on the disk fraction. , 67:120, December 2015. doi: 10.1093/pasj/psv094.
- J. Olofsson, M. Samland, H. Avenhaus, C. Caceres, T. Henning, A. Moór, J. Milli, H. Canovas, S. P. Quanz, M. R. Schreiber, J.-C. Augereau, A. Bayo, A. Bazzon, J.-L. Beuzit, A. Boccaletti, E. Buenzli, S. Casassus, G. Chauvin, C. Dominik, S. Desidera, M. Feldt, R. Gratton, M. Janson, A.-M. Lagrange, M. Langlois, J. Lannier, A.-L. Maire, D. Mesa, C. Pinte, D. Rouan, G. Salter, C. Thalmann, and A. Vigan.

- Azimuthal asymmetries in the debris disk around HD 61005. A massive collision of planetesimals? , 591:A108, June 2016. doi: 10.1051/0004-6361/201628196.
- M. Pan and H. E. Schlichting. Self-consistent Size and Velocity Distributions of Collisional Cascades. , 747:113, March 2012. doi: 10.1088/0004-637X/747/2/113.
- F. Perri and A. G. W. Cameron. Hydrodynamic instability of the solar nebula in the presence of a planetary core. , 22:416–425, August 1974. doi: 10.1016/0019-1035(74)90074-8.
- P. Plavchan, M. Jura, and S. J. Lipsky. Where Are the M Dwarf Disks Older Than 10 Million Years? , 631:1161–1169, October 2005. doi: 10.1086/432568.
- P. Plavchan, M. W. Werner, C. H. Chen, K. R. Stapelfeldt, K. Y. L. Su, J. R. Stauffer, and I. Song. New Debris Disks Around Young, Low-Mass Stars Discovered with the Spitzer Space Telescope. , 698:1068–1094, June 2009. doi: 10.1088/0004-637X/698/2/1068.
- D.H Rank, A.G.St Pierre, and T.A Wiggins. Rotational and vibration constants of co. *Journal of Molecular Spectroscopy*, 18(4):418 – 427, 1965. ISSN 0022-2852. doi: [https://doi.org/10.1016/0022-2852\(65\)90048-2](https://doi.org/10.1016/0022-2852(65)90048-2). URL <http://www.sciencedirect.com/science/article/pii/0022285265900482>.
- B. Reipurth, D. Jewitt, and K. Keil. Protostars and Planets V. *Protostars and Planets V*, 2007.
- J. H. Rhee, I. Song, B. Zuckerman, and M. McElwain. Characterization of Dusty Debris Disks: The IRAS and Hipparcos Catalogs. , 660:1556–1571, May 2007. doi: 10.1086/509912.
- A. Roberge and I. Kamp. *Protoplanetary and Debris Disks*, chapter 4. University of Arizona Press, December 2010.

- A. Roberge, A. J. Weinberger, S. Redfield, and P. D. Feldman. Rapid Dissipation of Primordial Gas from the AU Microscopii Debris Disk. , 626:L105–L108, June 2005. doi: 10.1086/431899.
- A. Roberge, I. Kamp, B. Montesinos, W. R. F. Dent, G. Meeus, J. K. Donaldson, J. Olofsson, A. Moór, J.-C. Augereau, C. Howard, C. Eiroa, W.-F. Thi, D. R. Ardila, G. Sandell, and P. Woitke. Herschel Observations of Gas and Dust in the Unusual 49 Ceti Debris Disk. , 771:69, July 2013. doi: 10.1088/0004-637X/771/1/69.
- A. Roberge, B. Y. Welsh, I. Kamp, A. J. Weinberger, and C. A. Grady. Volatile-rich Circumstellar Gas in the Unusual 49 Ceti Debris Disk. , 796:L11, November 2014. doi: 10.1088/2041-8205/796/1/L11.
- M. Rodono, G. Cutispoto, V. Pazzani, S. Catalano, P. B. Byrne, J. G. Doyle, C. J. Butler, A. D. Andrews, C. Blanco, E. Marilli, J. L. Linsky, F. Scaltriti, M. Busso, A. Cellino, J. L. Hopkins, A. Okazaki, S. S. Hayashi, M. Zeilik, R. Helston, G. Henson, P. Smith, and T. Simon. Rotational modulation and flares on RS CVn and BY Dra-type stars. I - Photometry and SPOT models for BY Dra, AU Mic, AR Lac, II Peg and V 711 Tau (= HR 1099). , 165:135–156, September 1986.
- K. Sadakane and M. Nishida. Twelve additional ‘Vega-like’ stars. , 98:685–689, July 1986. doi: 10.1086/131813.
- P. C. Schneider and J. H. M. M. Schmitt. X-raying the AU Microscopii debris disk. , 516:A8, June 2010. doi: 10.1051/0004-6361/201014038.
- É. Sezestre, J.-C. Augereau, A. Boccaletti, and P. Thébault. Expelled grains from an unseen parent body around AU Microscopii. , 607:A65, November 2017. doi: 10.1051/0004-6361/201731061.
- B. Sibthorpe, G. M. Kennedy, M. C. Wyatt, J.-F. Lestrade, J. S. Greaves, B. C. Matthews, and G. Duchêne. Analysis of the Herschel DEBRIS Sun-like star sample. , 475:3046–3064, April 2018. doi: 10.1093/mnras/stx3188.

- N. Siegler, J. Muzerolle, E. T. Young, G. H. Rieke, E. E. Mamajek, D. E. Trilling, N. Gorlova, and K. Y. L. Su. Spitzer 24 μm Observations of Open Cluster IC 2391 and Debris Disk Evolution of FGK Stars. , 654:580–594, January 2007. doi: 10.1086/509042.
- N. D. Thureau, J. S. Greaves, B. C. Matthews, G. Kennedy, N. Phillips, M. Booth, G. Duchêne, J. Horner, D. R. Rodriguez, B. Sibthorpe, and M. C. Wyatt. An unbiased study of debris discs around A-type stars with Herschel. , 445:2558–2573, December 2014. doi: 10.1093/mnras/stu1864.
- D. E. Trilling, G. Bryden, C. A. Beichman, G. H. Rieke, K. Y. L. Su, J. A. Stansberry, M. Blaylock, K. R. Stapelfeldt, J. W. Beeman, and E. E. Haller. Debris Disks around Sun-like Stars. , 674:1086–1105, February 2008. doi: 10.1086/525514.
- T. Tsukagoshi, M. Momose, M. Saito, Y. Kitamura, Y. Shimajiri, and R. Kawabe. First Detection of [C I] $^3\text{P}_1$ - $^3\text{P}_0$ Emission from a Protoplanetary Disk. , 802:L7, March 2015. doi: 10.1088/2041-8205/802/1/L7.
- F.C. van den Heuvel, W. Leo Meerts, and A. Dymanus. Rotational hyperfine spectrum of the nh radical around 1 thz. *Chemical Physics Letters*, 92(3):215 – 218, 1982. ISSN 0009-2614. doi: [https://doi.org/10.1016/0009-2614\(82\)80262-5](https://doi.org/10.1016/0009-2614(82)80262-5). URL <http://www.sciencedirect.com/science/article/pii/0009261482802625>.
- F. van Leeuwen. Validation of the new Hipparcos reduction. , 474:653–664, November 2007. doi: 10.1051/0004-6361:20078357.
- Z. Wahhaj, D. W. Koerner, and A. I. Sargent. High-Resolution Imaging of the Dust Disk around 49 Ceti. , 661:368–373, May 2007. doi: 10.1086/512716.
- J. J. Wang, J. R. Graham, L. Pueyo, E. L. Nielsen, M. Millar-Blanchaer, R. J. De Rosa, P. Kalas, S. M. Ammons, J. Bulger, A. Cardwell, C. Chen, E. Chiang, J. K. Chilcote, R. Doyon, Z. H. Draper, G. Duchêne, T. M. Esposito, M. P. Fitzgerald, S. J. Goodsell, A. Z. Greenbaum, M. Hartung, P. Hibon, S. Hinkley, L.-W. Hung, P. Ingraham, J. E.

- Larkin, B. Macintosh, J. Maire, F. Marchis, C. Marois, B. C. Matthews, K. M. Morzinski, R. Oppenheimer, J. Patience, M. D. Perrin, A. Rajan, F. T. Rantakyö, N. Sadakuni, A. Serio, A. Sivaramakrishnan, R. Soummer, S. Thomas, K. Ward-Duong, S. J. Wiktorowicz, and S. G. Wolff. Gemini Planet Imager Observations of the AU Microscopii Debris Disk: Asymmetries within One Arcsecond. , 811:L19, October 2015. doi: 10.1088/2041-8205/811/2/L19.
- J. P. Williams and L. A. Cieza. Protoplanetary Disks and Their Evolution. , 49:67–117, September 2011. doi: 10.1146/annurev-astro-081710-102548.
- D. J. Wilner, S. M. Andrews, M. A. MacGregor, and A. M. Hughes. A Resolved Millimeter Emission Belt in the AU Mic Debris Disk. , 749:L27, April 2012. doi: 10.1088/2041-8205/749/2/L27.
- G. Winnewisser, A. G. Maki, and D. R. Johnson. Rotational constants for hcn and dcn. *Journal of Molecular Spectroscopy*, 39(1):149 – 158, 1971. ISSN 0022-2852. doi: [https://doi.org/10.1016/0022-2852\(71\)90286-4](https://doi.org/10.1016/0022-2852(71)90286-4).
- G. Winnewisser, S.P. Belov, Th. Klaus, and R. Schieder. Sub-doppler measurements on the rotational transitions of carbon monoxide. *Journal of Molecular Spectroscopy*, 184(2):468 – 472, 1997. ISSN 0022-2852. doi: <https://doi.org/10.1006/jmsp.1997.7341>. URL <http://www.sciencedirect.com/science/article/pii/S0022285297973410>.
- M. Womack, G. Sarid, and K. Wierzbos. CO in Distantly Active Comets. , 129(3): 031001, March 2017. doi: 10.1088/1538-3873/129/973/031001.
- M. C. Wyatt. Evolution of Debris Disks. , 46:339–383, September 2008. doi: 10.1146/annurev.astro.45.051806.110525.
- M. C. Wyatt, O. Panić, G. M. Kennedy, and L. Matrà. Five steps in the evolution from protoplanetary to debris disk. , 357:103, June 2015. doi: 10.1007/s10509-015-2315-6.

-
- B. Zuckerman and I. Song. A 40 Myr Old Gaseous Circumstellar Disk at 49 Ceti: Massive CO-rich Comet Clouds at Young A-type Stars. , 758:77, October 2012. doi: 10.1088/0004-637X/758/2/77.
- B. Zuckerman, T. Forveille, and J. H. Kastner. Inhibition of giant-planet formation by rapid gas depletion around young stars. , 373:494–496, February 1995. doi: 10.1038/373494a0.